Carina Marisa dos Santos Almeida

Licenciada em Bioquímica

Gold nanoparticle-DNA conjugates for oligonucleotide vectorization towards gene silencing

Dissertação para obtenção do Grau de Mestre em
Genética Molecular e Biomedicina

Orientador: Prof. Doutor Pedro V. Baptista, Prof. Auxiliar, FCT-UNL

Júri:

Presidente: Prof. Doutor José Paulo Nunes de Sousa Sampaio
Arguente: Prof. Doutora Susana Isabel Rodrigues dos Santos
Vogal: Prof. Doutor Pedro Miguel Ribeiro Viana Baptista

FACULDADE DE CIÊNCIAS E TECNOLOGIA
UNIVERSIDADE NOVA DE LISBOA

Setembro 2011

Gold nanoparticle-DNA conjugates for oligonucleotide vectorization towards gene silencing

Resumo

O principal objectivo do trabalho apresentado nesta tese foi desenvolver um sistema de silenciamento génico usufruindo da capacidade de nanovectorização e propriedades ópticas das nanopartículas de ouro. A ideia baseia-se na construção de uma estrutura de DNA que contém um oligonucleotídeo terapêutico com capacidade de formar ligações de hidrogénio Hoogsteen com uma cadeia dupla de DNA, produzindo uma hélice tripla de DNA, para além de silenciar o gene de interesse. As ligações Hoogsteen, mais instáveis que as Watson-Crick convencionais, permitem alcançar temperaturas de *melting* mais baixas. Esta característica, aliada à capacidade de gerar calor através de irradiação com um laser nas nanopartículas de ouro utilizadas, vai permitir a libertação do oligonucleotídeo terapêutico e posterior silenciamento do gene de interesse sem aumento significativo da temperatura do meio. Assim, a tese apresenta três grandes secções: desenho e formação da estrutura de DNA, vectorização e silenciamento da expressão génica; as tarefas envolvidas nas diferentes secções foram efectuadas em paralelo.

O desenho da estrutura obtida teve em consideração a temperatura de *melting* desejável; estabilidade a condições fisiológicas dos nucleótidos formadores da sequência, número de ligações Hoogsteen e condições iónicas. Para avaliar a formação desta estrutura foram principalmente utilizadas técnicas de espectroscopia: análise de FRET e curvas de *melting* no ultra-violeta. Ambas as abordagens permitiram identificar interacções na presença do oligonucleotídeo terapêutico face à sua ausência, que poderão indicar a formação da estrutura. Para além disso, as curvas de *melting* permitiram a determinação da temperatura de libertação deste oligonucleotídeo – 40ºC. A funcionalização de DNA em dupla cadeia às nanopartículas de ouro foi conseguida, mas não se observaram diferenças na migração electroforética quando os três oligonucleotídeos estavam presentes. Contudo, o oligonucleotídeo terapêutico demonstrou capacidade de inibição eficiente da expressão génica em ensaios de transcrição e tradução *in vitro* com uma eficiência até 95% e 60%, respectivamente.

Palavras-chave: silenciamento génico; DNA *antisense*; nanopartículas de ouro; hélices triplas de DNA; nanovectorização.

Abstract

The main objective of the work presented in this thesis was to develop a gene silencing system by taking advantage of the nanovectorization capability and optical properties of gold nanoparticles. The idea is based on the construction of a DNA structure containing a therapeutic oligonucleotide with the ability to form Hoogsteen hydrogen bonds with double-stranded DNA, producing a DNA triple helix, besides silencing the gene of interest. Hoogsteen bonds, more unstable than the conventional Watson-Crick bonds, permit the achievement of lower melting temperatures. This attribute, coupled with the ability to generate heat by laser irradiation of the gold nanoparticles used, will allow the release of the therapeutic oligonucleotide and subsequent gene silencing without significant increase in the medium's temperature. Thus, the thesis comprises three major sections: structure design and formation, vectorization, and gene expression silencing; the tasks involved in each of these sections were conducted in parallel.

The design of the obtained structure took into account the desired melting temperature, stability at physiological conditions of the sequence-forming nucleotides, the number of Hoogsteen bonds and ionic conditions. To evaluate the formation of this structure, spectroscopic techniques were mainly used: FRET analysis and ultraviolet melting curves. Both approaches allowed the identification of interactions in the presence of therapeutic oligonucleotide compared with its absence, which may indicate structure formation. In addition, melting curves allowed the determination of the temperature of release of this oligonucleotide – 40ºC. The double-stranded DNA functionalization to gold nanoparticles has been achieved, but there was no difference in electrophoretic migration when the three oligonucleotides were present. However, the therapeutic oligonucleotide was able to efficiently inhibit gene expression in *in vitro* transcription and translation assays with efficiency up to 95% and 60% respectively.

Key-words: gene silencing; antisense DNA; gold nanoparticles; DNA triple helices; nanovectorization.

Table of Contents

Figure Index

Table Index

Symbols and Notations

ε – extinction coefficient
λ_{em} – emission wavelength
λ_{exc} – excitation wavelength
Φ_f – fluorescence quantum yield
A – adenine
AuNP – gold nanoparticle
C – cytosine
DNA – deoxyribonucleic acid
DNase – deoxyribonuclease
dsDNA – double strand DNA
dsRNA – double strand RNA
DTT – dithiothreitol
FAM – 6-carboxyfluorescein
FRET – Förster resonance energy transfer
G – guanine
GFP – green fluorescent protein
JOE – 6-carboxy-4′,5′-dichloro-2′,7′-dimethoxyfluorescein
LSPR – localized surface plasmon resonance
mRNA – messenger RNA
MYC – human v-myc myelocytomatosis viral oncogene homolog
NP – nanoparticle
PAGE – polyacrylamide gel electrophoresis
PCR – polymerase chain reaction
PEG – polyethylene glycol
RBS – ribosome binding site
RISC – RNA-induced silencing complex
RNA – ribonucleic acid
RNAi – RNA interference
RNase – ribonuclease
siRNA – small interfering RNA
SPR – surface plasmon resonance
ssDNA – single strand DNA
T – timine
TEM – transmission electron microscopy
TFO – triplex-forming oligonucleotide
T_m – melting temperature
tsDNA – triple strand DNA
UV – ultraviolet

1. Introduction

The work here presented, although solely focused on gene therapy, is a small part of a larger project whose central focus is on nanotheranostics.

1.1. Nanotheranostics

Theranostics is the combination of real-time diagnotics with delivery of medication (Prigodich *et al.*, 2009; Ho and Leong, 2010; Lukianova-Hleb *et al.*, 2010; Xie *et al.*, 2010) and aims to make a treatment shorter, safer and more efficient through selective targeting of specific (diseased) tissues or cells. However, the initial phase of the development of theranostics has already revealed two main challenges: (i) lack of multifunctional methods and agents; and (ii) deficient selectivity and specificity of available agents (Lukianova-Hleb *et al.*, 2010).

Over the last decade, several multifunctional approaches have been employed as theranostic agents, such as: fluorescent dyes, capsule-type sytems (liposomes, micelles, polyelectrolyte and polymer capsules) and nanotechnological materials (especially nanoparticles; NPs). Taking advantage of the potential of certain materials at the nanometer scale, and hence of nanotechnology, appears to be the most advantageous and effective approach for the combination of diagnosis and therapy in a single system. Several reports of the use of nanotechnology for application in theranostics (nanotheranostics or theranostic nanomedicine) have already been presented (Bagalkot *et al.*, 2007; Medarova *et al.*, 2007; Park *et al.*, 2008; Yezhelyev *et al.*, 2008; Prigodich *et al.*, 2009; Ho and Leong, 2010; Lukianova-Hleb *et al.*, 2010).

1.2. Nanotechnology

Nanotechnology is a multidisciplinary scientific field that involves the study, creation and control of matter on the nanometer (one billionth of a meter) scale.

Since the discovery of their quantum size effects, biomedical applications and methods of manufacturing, NPs are one of the most explored and employed class of nanomaterials (Salata, 2004; Kotov and Stellacci, 2008). NPs can be composed of one or more inorganic compounds such as noble metals, heavy metals, iron, etc. (Niemeyer and Mirkin, 2004). In particular, noble metal NPs have been attracting much interest due to their simplicity, versatility, easily tunable physicochemical properties and high surface areas which make them suitable for many biological applications (Baptista *et al.*, 2008; Wilson, 2008). These properties are mainly dependent on their size, shape and composition (Su *et al.*, 2003).

Among noble metal NPs, gold nanoparticles (AuNPs) have been subject of extensive research and, in the last years, led to the development of a myriad of techniques and methods for diagnostics, imaging, drug delivery and therapeutics (Hu *et al.*, 2006; Baptista *et al.*, 2008; Sperling *et al.*, 2008; Boisselier and Astruc, 2009; Huang and El-Sayed, 2010). This widespread use of AuNPs is the consequence of two important properties for biomedical application: unique optical properties and ease of surface functionalization.

1.2.1. Optical properties

One of the most studied properties of AuNPs is their interaction with light. The free surface electrons of the AuNP undergo a collective coherent oscillation on its surface when in the presence of the electromagnetic waves of the light. At a particular frequency of the light, this process is resonant and is termed the localized surface plasmon resonance (LSPR) oscillation (Eustis and El-Sayed, 2006). The LSPR frequency for spherical AuNPs with diameters between 10-100 nm lies in the visible region of the electromagnetic spectrum (Jain *et al*., 2007) due to the similar quantum confinement of the nanoparticle for the oscillating electrons and the incident radiation wavelength (El-Sayed, 2001). The LSPR can be tuned by modification of the nanostructure size, shape, composition or the dielectric constant of the surrounding medium (Jain *et al.*, 2006; P.K. Jain *et al.*, 2008) in order to suit the biomedical application.

Plasmon oscillations in a NP can either decay by radiating its energy resulting in light scattering, or non-radiatively as heat (P.K. Jain *et al*., 2008). Only the latter mechanism of dissipation is covered under the scope of this work.

AuNPs are thought to generate heat by light activation and these heaters are useful for applications in biomedicine because temperatures above 37ºC lead to fever and temperatures higher than 42ºC are lethal to human cells. The increase in temperature in the vicinity of AuNPs' surface can be explained by the optical near-field effect and that increase is a function of the distance from AuNPs' surface (Govorov *et al.*, 2006; Govorov and Richardson, 2007) as shown in Figure 1.1.

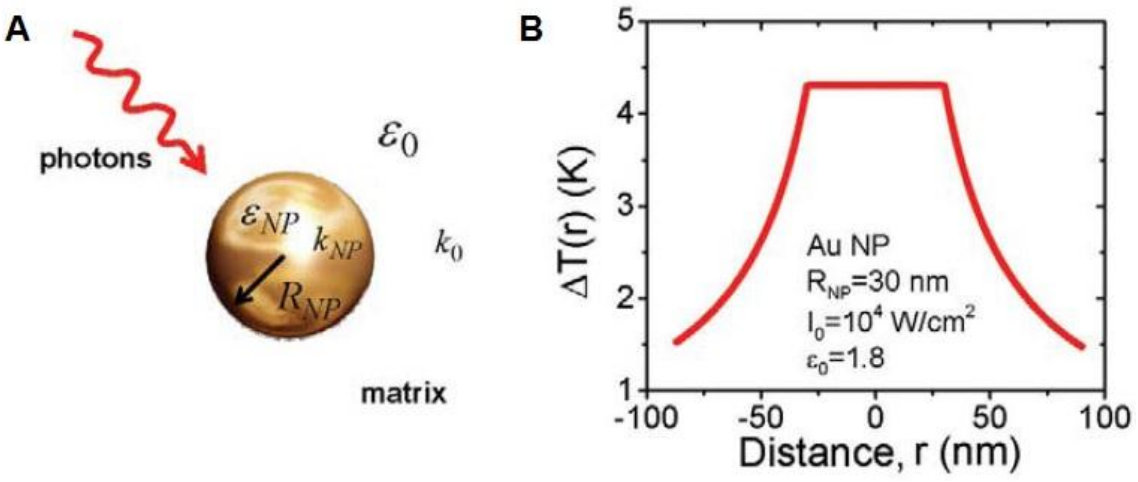

Figure 1.1 – A) Scheme of an optically driven spherical nanoparticle. B) Temperature increase for a single AuNP as a function of the distance from its center and with water as surrounding medium. ε_{NP} and ε_0 are the dielectric constants of the NP and surrounding medium, respectively; R_{NP} is the NP radius; k_{NP} and k_0 are the thermal conductivity of the NP and surrounding medium, respectively; and I_0 is the light intensity inside the matrix (Govorov and Richardson, 2007).

This property has been especially exploited as anti-cancer therapy by the selective laser photothermolysis of malignant cells. AuNPs conjugated to ligands that are specific to receptors overexpressed on cancer cells can be selectively targeted to cancer cells without significant binding to healthy cells (Hu *et al.*, 2006; P.K. Jain *et al.*, 2008; Sperling *et al.*, 2008). Upon irradiation with a laser

of frequency overlapping the LSPR absorption maximum, the absorbed light is rapidly converted into heat and there is a selective heating and destruction of cancer cells at much lower laser powers than those required to destroy healthy cells to which nanoparticles do not bind specifically (P.K. Jain *et al.*, 2008; Boisselier and Astruc, 2009).

Photothermal therapy using AuNPs requires much lower laser energies than conventional dyes due to AuNPs' 5-fold higher absorption coefficients, which make them minimally invasive (Chen *et al.*, 2008; P.K. Jain *et al.*, 2008). While the use of visible light resonant AuNPs can be useful for external skin/surface cancer treatments (Huang and El-Sayed, 2010), for tumors within bodily tissue, it becomes necessary to use near-infrared light in the biological window (Hu *et al.*, 2006; P.K. Jain *et al.*, 2008; Boisselier and Astruc, 2009).

Although photothermolysis is the most common application of nanotechnology for cancer therapy, one can use this property to achieve the displacement of therapeutic moieties functionalized to the NPs' surface and achieve a therapeutic action by means of gene silencing (Huschka *et al.*, 2010; Poon *et al.*, 2010).

1.2.2. Therapy nanovectorization

Therapeutic vectors may carry drugs, genes and imaging agents into living cells and tissues. Over the years, several different vehicles for delivery have been designed based on different nanomaterials, such as polymers, dendrimers, liposomes, nanotubes, nanorods, etc (Ghosh *et al.*, 2008). The use of nanovectors allows the specific delivery of large amounts of therapeutic agents per targeting biorecognition event, constituting a major clinical advantage of this approach. Moreover, nanovectors are capable of reducing the clearance time of therapeutic agents and provide protection against enzymatic degradation (Ferrari, 2005). AuNPs provide excellent characteristics for nanovectorization of drug molecules or large biomolecules (e.g. proteins or nucleic acids) due to their high surface/volume ratio and ease of functionalization via conventional and/or simple processes. Also, gold is essentially inert and non-toxic (Murphy *et al.*, 2008).

The delivery of therapeutic nucleic acids appears to be very promising. An ideal vector must possess the following properties: easy production; ability to express its genetic cargo over a sustained period; immunologically inert; tissue/cell-specific; ability to infect dividing and non-diving cells; no size limit to the genetic material it can deliver (Somia and Verma, 2000). Hitherto, most gene therapies have been based on viral vectors because viruses have the mechanisms to transfer their DNA into host cells, making them ideal for delivering external genetic material into tumor cells. However, the use of common viral vectors raises cytotoxicity and adverse immune responses in humans (Waehler *et al.*, 2007; Boisselier and Astruc, 2009).

AuNPs can be used as synthetic delivery vectors that have already proven successful in delivering large biomolecules such as peptides, proteins, and nucleic acids, and unlike viruses, AuNPs are inert to the organism, although less efficient than viral vectors (Ghosh *et al.*, 2008).

Delivery of DNA by means of AuNPs has been developed first by Rotello's group using cationic ligands (McIntosh *et al.*, 2001) and then with amphiphilic ligands that were more efficient on

transfection (Ghosh *et al.*, 2008). Rosi *et al.* have conjugated AuNPs with negatively-charged oligodeoxynucleotides using antisense oligonucleotides (Rosi *et al.*, 2006) and AuNPs conjugated with siRNA (Giljohann *et al.*, 2009) for gene therapy. Rotello *et al.* also reported another approach to gene delivery by means of AuNPs-directed photorelease of oligonucleotides where, upon ultraviolet (UV) irradiation within the cells, DNA is released from AuNPs resulting in a high level of DNA-transcription recovery *in vitro,* and with significant nuclear localization of the DNA in cells (Han *et al.*, 2006).

In the last years, the use of NPs for photothermal therapy (see section 1.2.1) and/or as suitable vehicles to act as vectorization platforms (see section 1.2.2) has raised much interest in the treatment and/or prevention of cancer (Cheng *et al.*, 2009; Bardhan *et al.*, 2011; Gianella *et al.*, 2011; Ke *et al.*, 2011; Melancon *et al.*, 2011). This is due to the enhanced permeability of tumor vasculature and cancer markers that facilitate retention of NPs within a tumor coupled with the increasing burden of this disease worldwide.

1.3. Cancer therapy

Cancer is among the major causes of mortality in the developed world, and the worldwide incidence continues to increase. The mainstay of treatment for cancer is surgery, radiation, chemotherapy, antibody-blocking therapy, or a combination of these therapies. These methods are invasive (e.g. surgery) and/or hazardous due to lack of selectivity to cancerous cells or tissue (e.g. chemotherapy, radiotherapy). Although cancer treatment is improving and extending survival rate for people with cancers at many sites, there is a need to reduce the impact of highly toxic agents to healthy tissue. Also, the poor bioavailability seriously compromises the therapeutic efficacy of many otherwise beneficial drugs (Chen *et al*., 2008). These treatments also inhibit growth and development of blood cell lineages, ultimately leading to increased susceptibilities to secondary infections.

To surmount at least some of these challenges, alternative non-invasive and selective methods are being exploited and developed. In particular, gene therapy is receiving increasing attention and could represent an attractive approach for novel treatment and/or prevention of cancer by the controlled introduction of therapeutic nucleic acids into target cells in order to block the expression of specific genes. Gene expression can be regulated at either the transcriptional or post-transcriptional level. At the transcriptional stage, oligonucleotides must enter the nucleus of a cell and specifically bind to the RNA polymerase promoter of double-stranded genomic DNA to form triple helices that prevent transcription (Tamm *et al*., 2001; Patil *et al.*, 2005; Rayburn and Zhang, 2008). At the post-transcriptional level, antisense oligonucleotides and small interfering RNA (siRNA) are available for the sequence-specific gene silencing.

1.4. Gene silencing

RNA interference (RNAi) is the phenomenon that triggers degradation of messenger RNA (mRNA) complementary to either strand of a short double-stranded RNA (dsRNA; Lewin, 2007). In theory, the

RNAi machinery can be exploited to silence nearly any gene, giving it a broad therapeutic potential (Whitehead *et al.*, 2009).

The general mechanism of RNAi is triggered by the presence of long pieces of dsRNA and involves the cleavage of these molecules into regulatory molecules of twenty-one to twenty-three bases with short (two base) protruding 3'-ends by Dicer. In practice, siRNA can be synthetically produced and then directly introduced into the cell, thus circumventing Dicer mechanics.

Once siRNA is present in the cytoplasm of the cell, it is incorporated into a ribonuclear protein complex known as the RNA-induced silencing complex (RISC). Within the RISC complex exists a member of the Argonaute protein family (in mammalian cells, the protein is Ago2) which unwinds the siRNA. The activated RISC, which contains the antisense strand of the siRNA as a template (the sense strand is cleaved), selectively degrades mRNA that is complementary to the antisense strand (Hammond *et al.*, 2001; Hannon and Rossi, 2004; Meister and Tuschl, 2004; De Paula *et al.*, 2007; Whitehead *et al.*, 2009; Kim *et al.*, 2005). The homologous mRNA, upon binding to RISC, is cleaved between bases 10 and 11 relative to the 5′-end. The activated RISC complex can then undergo numerous cycles of mRNA cleavage, which further propagates gene silencing (De Paula *et al.*, 2007; Whitehead *et al.*, 2009). A schematic representation of the siRNA pathway is depicted in Figure 1.2.

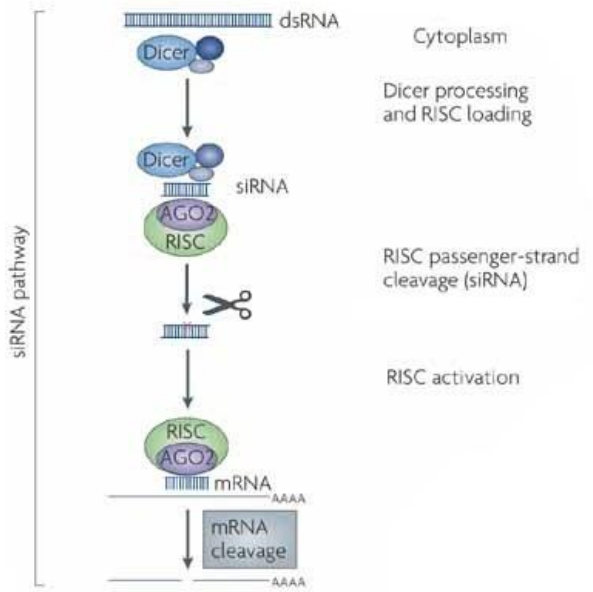

Figure 1.2 – The siRNA pathway in mammalian cells (adapted from de Fougerolles *et al.*, 2007). dsRNA is cleaved into siRNAs by Dicer. These fragments are then incorporated in RISC, which becomes activated by the presence of the antisense strand of the siRNA. This complex is capable of mRNA degradation complementary to the antisense strand of siRNA.

Antisense silencing is based on single-stranded oligonucleotide sequences that are specifically designed to hybridize to corresponding mRNA and inhibit its function by modulation of splicing or disruption of ribosome assembly (Tamm *et al.*, 2001; Patil *et al.*, 2005). Therefore, there is a potential role for antisense oligonucleotides in the treatment of disease.

Antisense oligonucleotides and siRNA show significant potential in new molecular approaches to down-regulate specific gene expression in cancer. However, there are still significant obstacles to be overcome before their use as anticancer agents in clinical applications. Naked oligonucleotides show extremely short half-lives (seconds to minutes) when delivered into the bloodstream due to renal clearance (because of their small size) and to RNase and DNase action. Also, the cellular uptake of naked oligonucleotides is limited (Oliveira *et al.*, 2006; Pirollo and Chang, 2008). Therefore, the efficiency of these approaches for cancer therapy relies on finding suitable delivery vectors that can be systemically administered to reach both primary and metastatic tumor cells. Several different vectorization approaches have been developed based on nonviral lipids or protein carriers, including cholesterol, liposomes, antibody protomer fusions, cyclodextrin nanoparticles, fusogenic peptides, aptamers, biodegradable polylactide copolymers, and polymers (Pirollo and Chang, 2008). Positively charged cationic liposomes and polymers, such as polyethyleneimine, are currently the two major carriers used to complex with negatively charged oligonucleotides for systemic delivery (Oliveira *et al.*, 2006; De Paula *et al.*, 2007).

1.5. DNA triple helices

The DNA double strand is formed by two complementary strands, where an adenine (A) pairs with thymine (T) and guanine (G) with cytosine (C) forming A•T and G•C base pairs through Watson-Crick hydrogen bonds. However, in the DNA major groove, acceptor and donor groups are spatially available to form hydrogen bond interactions with a third external strand. The hydrogen bond interactions involved in triple-helix formation are a less stable hydrogen-bonding pattern, referred to as Hoogsteen hydrogen bonds (Chan and Glazer, 1997; Duca *et al*., 2008).

There are several requisites for triplex formation – it occurs when a DNA or RNA oligonucleotide binds specifically to the major groove of a homopurine region of DNA. A triplex-forming oligonucleotide (TFO) can be categorized in either the pyrimidine or purine motif, depending on its base composition and binding orientation relative to its DNA target site.

A TFO formed by C and T binds parallel to the purine-rich strand of DNA via Hoogsteen bonds in a pyrimidine motif. Ts belonging to the third strand bind to A in A:T basepairs and protonated Cs (C+) bind to G in G:C+ basepairs. Because the protonation at N3 of C is required for proper Hoogsteen bonding with N7 of G, the pyrimidine motifs occur only under acidic conditions (pH < 6). This imposes a limitation to the use of pyrimidine oligonucleotides at physiologic pH without further modification (Chan and Glazer, 1997; Duca *et al.*, 2008).

In the purine motif, the TFO consists of As and Gs which bind to the purine-rich strand of DNA by A:T, G:C and A:A Hoogsteen hydrogen basepairs. These TFOs bind antiparallel to the purine-rich strand in DNA and unlike the pyrimidine motif, the purine motif requires no base protonation and exhibits pH independent binding (Chan and Glazer, 1997; Duca *et al.*, 2008). Figure 1.3 shows these two motifs and the hydrogen bonds that each one form.

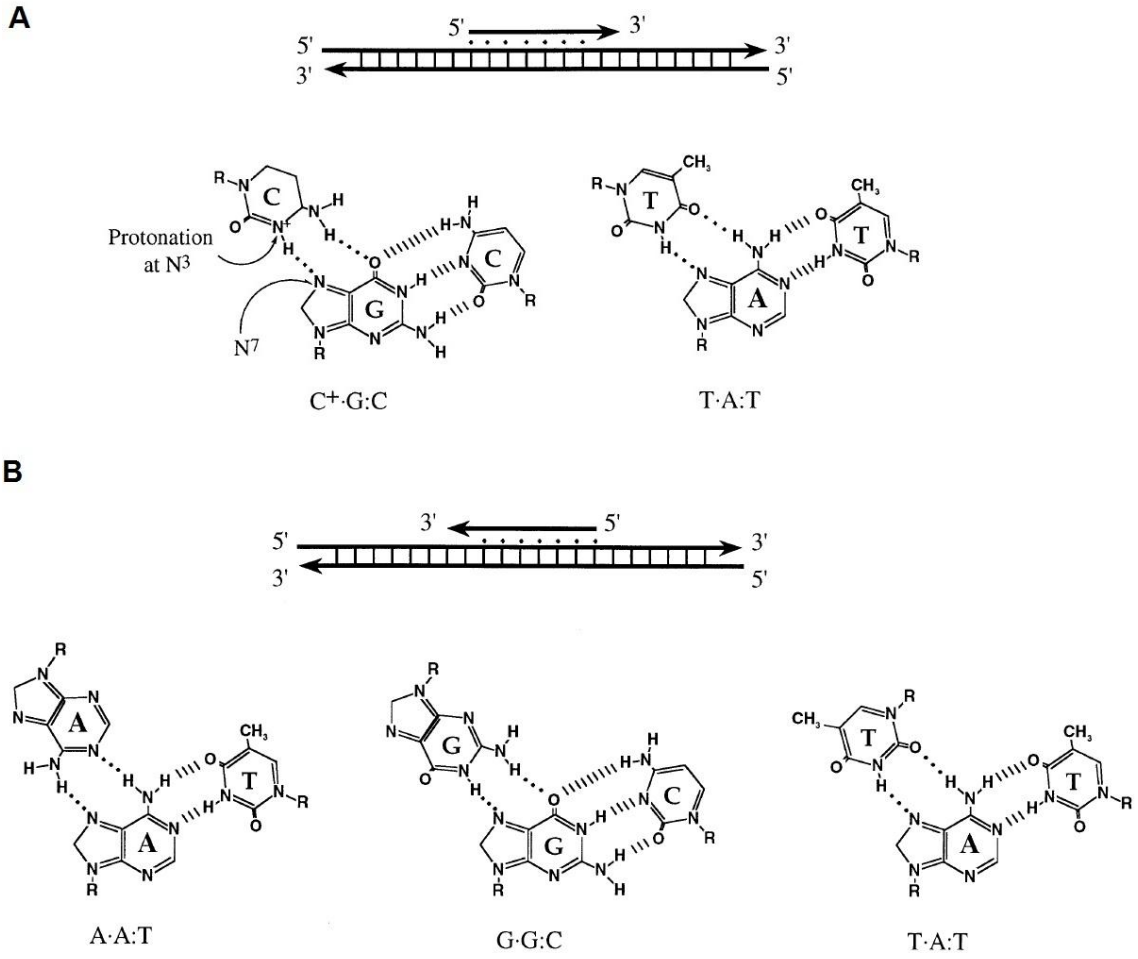

Figure 1.3 – Motifs in triplex DNA formation and hydrogen bonding. A) Pyrimidine binding motif. Above: binding of a TFO in a parallel orientation to a polypurine strand of DNA; Below: the two canonical base triplets of this motif. **B)** Purine binding motif. Above: binding of a TFO to the polypurine strand of DNA in an antiparallel orientation; Below: three canonical base triplets in this motif. · represent Hoogsteen hydrogen bonds; **|** represent Watson-Crick hydrogen bonds (adapted from Chan and Glazer, 1997).

The affinity to which a TFO binds to a polypurine site depends on the TFO sequence: purine motifs must generally be G-rich (>65%) to form stable triplexes; for the pyrimidine motif, a high percentage of Cs appears to be destabilizing. The presence of divalent cations such as Mg^{2+}, Ca^{2+} and Zn^{2+} stabilize both purine and pyrimidine motifs (Chan and Glazer, 1997; Wu *et al.*, 2002). Spermine, spermidine and putrescine are naturally occurring polyamines that also improve the stability of triple helices. These agents reduce the electrostatic repulsive forces between the negatively charged phosphate backbones of the three strands, allowing triplex DNA to form more readily (Chan and Glazer, 1997).

To overcome the lack of stability, base analogs can be introduced, the sugar moiety modified, as well as the backbone or chemical substances, known to enhance the formation of triplex DNA (Knauert and Glazer, 2001; Duca *et al.*, 2008; A. Jain *et al.*, 2008), can be used.

There are many potential applications for TFOs including site-directed mutagenesis, induced recombination and transcriptional and post-transcriptional inhibition (Mukherjee and Vasquez, 2011).

1.6. Objectives

The work here presented focus on the use of AuNPs as nanovectors for gene silencing. In order to achieve the silencing, suitable single-stranded oligonucleotides (ssDNA) and/or siRNA are aimed to be entrapped in specifically designed tertiary nucleic acid structures that are further functionalized to the AuNPs' surface. The entrapment will be accomplished by Hoogsteen hydrogen bonds between a trapping double helix DNA structure and part of the effector ssDNA and/or siRNA, forming a triple helix of DNA.

The use of a DNA triplex structure will allow for the use of lower laser energies to achieve the melting of the effector strand when compared to simple double stranded constructs. The melting temperature of the third strand from the entrapment oligonucleotide will be designed in such a way to be released at temperatures just above physiological temperature, i.e., the triplex structure should be stable enough until laser irradiation, and the laser energy will be low enough to prevent damage in the surrounding cells.

In the present work, the delivery of oligonucleotides might be achieved via the release from the trapping molecule through spectral interaction (e.g. near-field effect, thermal effect) with/and between the AuNPs. The AuNPs conjugated with the triplex structure will be irradiated by a laser, increasing the temperature on the surface of the AuNPs. This increase will lead to thermal denaturation of the triplex structures conjugated with the AuNP, releasing the entrapped oligonucleotide within the cell. The naked oligonucleotide will thereafter achieve the silencing of its target (see Figure 1.4 for a schematic representation).

Towards the completion of the referred objectives, the work was planned in the following consecutive tasks:

- Design of triplex DNA structures in which a domain of the double-stranded DNA (dsDNA) chain is capable of entrapping a third-strand effector oligonucleotide. The length of the triple helix section will be designed to satisfy the thermal denaturation profiles attained via the near-field effect of AuNPs;
- *in vitro* temperature effect assessment on the release of entrapped oligonucleotides via Förster resonance energy transfer (FRET) analysis and UV melting profiles;
- Optimization of silencing conditions for antisense and siRNA approach;
- Synthesis of AuNPs and functionalization of the triplex structure onto the AuNPs' surface;
- Assessment of release via thermal denaturation and/or target silencing.

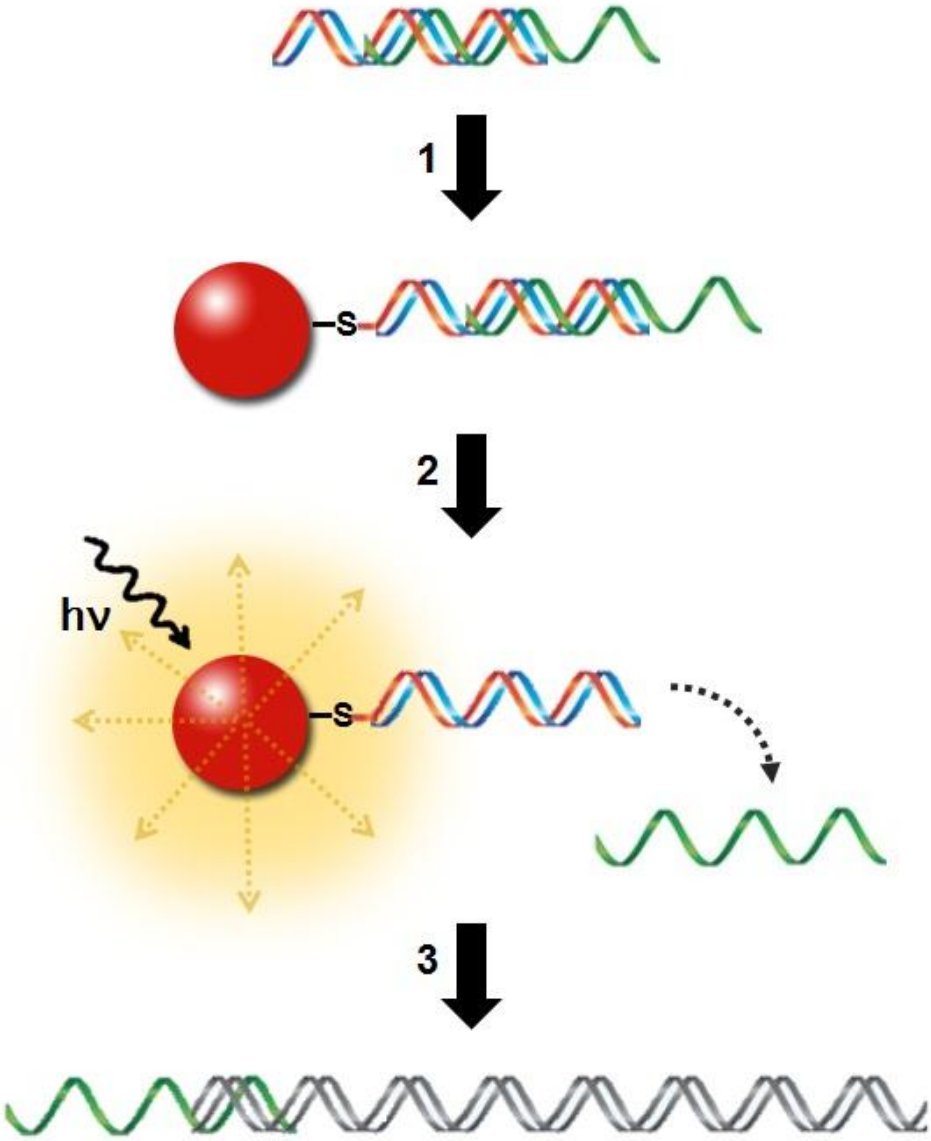

Figure 1.4 – Schematic representation of the project. 1) Functionalization of the triplex DNA structure to AuNPs via thiol group after previous assessment of triplex structure formation entrapping the therapeutic oligonucleotide (represented in green); **2)** Release of the therapeutic oligonucleotide – laser irradiation of AuNPs and consequent thermal denaturation of the third strand; **3)** Gene silencing by the released therapeutic oligonucleotide.

2. Materials and Methods

2.1. General information

All chemicals were purchased from Sigma-Aldrich in the highest purity available and used without further purification. All synthetic oligonucleotides were purchased from STAB Vida, Lda. (Portugal) and their sequences are shown in Table 2.1.

Table 2.1 – Unmodified and modified DNA oligonucleotides and their melting temperatures (T_m) according to the nearest neighbor model.

Designation	Sequence (5' to 3')	T_m (ºC)	Modification	Function
1T17	GGGGAGGAAGAGAAGAAAGAA	51.7		Triplex formation
1T17_5'thiol_3'FAM			5'-thiol-$(CH_2)_6$ 3'-FAM	Vectorization
2T17	TTCTTTCTTCTCTTCCTCCCC	51.7		Triplex formation
2T17_5'FAM			5'-FAM	Triplex formation
2T17_5'JOE			5'-JOE	Vectorization
3T17	CATGGTATATTTGTTTGTTGTGTTGGT	53.5		Triplex formation
3T17_11dT-JOE			T_{11}-JOE	Triplex formation
3T17_T7	TCTCCCTATAGTGAGTCGTATTATTGTTTGTTGTGTTGGT	64.0		Inhibition of *in vitro* transcription
3T17_RBS	CATGGTATATCTCCTTCTTATTGTTTGTTGTGTTGGT	61.5		Inhibition of *in vitro* translation
MYCreverse	AGGCAGTTTACATTATGGCTAAATC	53.7		PCR primer
T7–MYCforward	TAATACGACTCACTATAGGGAGAGCTCATTTCTGAAGAGGACTTGT	69.0		PCR primer
Non-TFO	TAGACGGTGGTGCAAATAGTAACGG	57.8		Triplex formation control

2.2. DNA structure formation and assessment

2.2.1. FRET analysis

T17 structure (*vide* Figure 3.1) formation was attempted in a binding buffer (10 mM Tris-HCl, pH 7.6; TE 1x, pH 7.0; or 10 mM sodium phosphate, pH 7.4) with certain concentrations of $MgCl_2$ or $MnCl_2$ and/or NaCl and the concentration of each oligonucleotide (1T17, 2T17_5'FAM and 3T17_11dT-JOE) was set to 1 μM. Two of the oligonucleotides used (2T17_5'FAM and 3T17_11dT-

JOE) are labeled with one fluorophore each: FAM and JOE, respectively, whose emission and absorption spectra and quantum yields are shown in Figure 2.1.

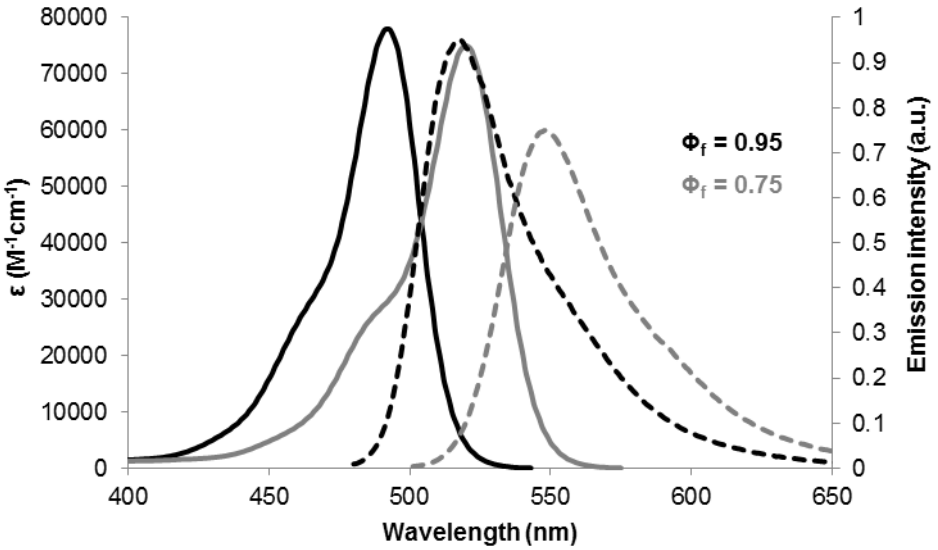

Figure 2.1 – Absorption and emission spectra of FAM and JOE. Black lines correspond to FAM and grey lines to JOE. Absorption spectra are represented by solid lines normalized to the extinction coefficients (ε) and emission spectra are represented by the dashed lines normalized to the fluorescence quantum yields (Φ_f).

Oligonucleotides were denatured for 10 min at 80ºC followed by gradual cooling to 4ºC at a rate of 0.1ºC/min. The experiments were performed at 15ºC in order to guarantee that a triplex can be formed if the necessary requirements are met. Emission and excitation spectra were measured using a fluorescence spectrophotometer Cary Eclipse with Peltier thermostat accessory (Varian, USA). The excitation wavelength (λ_{exc}) of FAM was set to 490 nm and the emission intensity was scanned between 500 and 700 nm. To record the excitation spectra, the emission wavelength (λ_{em}) was set to 640 nm and the intensity between 400 and 650 nm was recorded. The absorption spectra were measured using a UV-Vis spectrophotometer Evolution 300 with Peltier thermostat accessory (Thermo Scientific, USA).

2.2.2. Melting profile

UV melting curves for T17 structure were recorded in 10 mM Tris-HCl and 10 mM $MgCl_2$ where the concentration of each oligonucleotide (1T17, 2T17 and 3T17) was set to 2 μM. The melting curve was recorded at 260 nm from 25 to 85ºC at a scan rate of 1ºC/min using a UV-Vis spectrophotometer Evolution 300 with Peltier thermostat accessory (Thermo Scientific, USA).

2.3. Synthesis of colloidal AuNPs (adapted from Lee and Meisel, 1982)

AuNPs were prepared by the citrate reduction method previously described. Briefly, 250 mL of 1 mM HAuCl4 was brought to a boil while stirring in a 500 mL round-bottom flask. While in reflux, 25 mL

of 38.8 mM sodium citrate was quickly added and the mixture was kept refluxing for 15 min with continuous stirring. The colloidal solution was left to cool to room temperature and stored in the dark until use. AuNPs concentration was determined by the Lambert–Beer law assuming a calculated molar absorptivity for the plasmon resonance band maximum of 2.33×108 $M^{-1}cm^{-1}$. The average size and morphology of the particles were obtained by analysis of transmission electron microscopy (TEM) images.

2.4. Synthesis of dsDNA-AuNP conjugates

After resuspension of the thiol-modified oligonucleotide (1T17_5'thiol_3'FAM) in 0.1 M dithiothreitol (DTT), one volume was extracted with two volumes of ethyl acetate and the organic phase was discarded after centrifuging for 5 minutes at 21,460 g. This procedure was repeated two more times. The aqueous phase was further purified through a desalting NAP-5 column (GE Healthcare, USA) according to manufacturer's instructions, using 10 mM phosphate buffer as eluent. The purified oligonucleotide was then quantified by UV-visible spectroscopy using the extinction coefficient at 260 nm provided by the manufacturer and subsequently mixed with its complementary sequence (2T17_5'JOE). The mixture was denatured at 70ºC for 10 min and then allowed to hybridize for 15 min at room temperature.

After these steps, several methods of dsDNA conjugation to AuNPs were employed as described below.

2.4.1. Incubation of AuNPs and dsDNA (adapted from Sato *et al.* 2003)

The pre-hybridized dsDNA was mixed with a 15 nM AuNPs solution in a 1:100 (AuNP:dsDNA) ratio. After a minimum of 48 hours at room temperature, the functionalized AuNPs were centrifuged at 21,460 g for 20 min. The supernatant was discarded and the resulting oily pellet was washed twice with 10 mM phosphate buffer (pH 8.0) and finally redispersed with the same solution. The final concentration of dsDNA-AuNPs conjugates was determined by the Lambert–Beer law assuming a calculated molar absorptivity for the plasmon resonance band maximum of 2.33×108 $M^{-1}cm^{-1}$. The dsDNA-AuNPs conjugates were stored in the dark at 4ºC until further use.

2.4.2. Salt-aging method (adapted from Hurst *et al.*, 2006)

The pre-hybridized dsDNA was mixed with a colloidal solution of AuNPs in a 1:200 (AuNP:dsDNA) ratio. The mixture were brought to 10 mM sodium phosphate buffer (pH 8.0) and 0.01% SDS and allowed to incubate at room temperature for 20 min. NaCl concentration was increased to 0.05 M using 10 mM sodium phosphate buffer (pH 8.0), 1.5 M NaCl and 0.01% SDS, followed by incubation at room temperature for 20 min. This process was repeated to reach final concentrations of NaCl of 0.1 M, 0.2 M and 0.3 M. After 16 hours of incubation at room temperature, the excess of oligonucleotides were removed by centrifugation and removal of the supernatant and this process was repeated three times. The final pellet was resuspended in 10 mM sodium phosphate buffer (pH 8.0)

and 0.1 M NaCl. The final concentration of dsDNA-AuNPs conjugates was determined by the Lambert–Beer law assuming a calculated molar absorptivity for the plasmon resonance band maximum of 2.33×108 $M^{-1}cm^{-1}$. The dsDNA-AuNPs conjugates were stored in the dark at 4ºC until further use.

2.5. Determination of dsDNA-AuNPs hybridization efficiency (adapted from Demers *et al.*, 2000)

The dsDNA-AuNPs conjugates (final concentration 5 nM) was denatured using sodium hydroxide (final concentration of 0.1 M; final pH of 13) in a total volume of 100 µL of 10 mM phosphate buffer (pH 8.0) and let to incubate for 2 h at room temperature. The calibration curve was generated by preparing a sequential dilution of the JOE-modified oligonucleotide (2T17_5'JOE; concentration range: 0.01 – 0.5 µM) under the same conditions as the samples.

The samples were then centrifuged at 21,460 g for 20 min and the supernatant was removed to measure the fluorescence emission of the sample in a Cary Eclipse with Peltier thermostat accessory (Varian, USA). Sample's fluorescence emission was converted to molar concentrations by interpolation from the standard linear calibration curve.

2.6. Quantitation of thiol-modified oligonucleotides loaded on AuNPs (adapted from Sato *et al.*, 2003)

Thiol- and FAM-modified oligonucleotides (1T17_5'thiol_3'FAM) were displaced from the AuNPs' surface via addition of DTT (final concentration of 100 mM) or β-mercaptoethanol (final concentration of 12 mM) to 5 nM dsDNA-AuNPs conjugates (pellet obtain in the assay described in 2.5) in a total volume of 100 µL. Standard solutions were prepared by sequentially diluting (concentration range: 0.01 – 0.5 µM) the thiol- and FAM-modified oligonucleotide (1T17_5'thiol_3'FAM) under the same conditions as the samples. After 48 hours at room temperature, samples were centrifuged at 21,460 g for 20 minutes and then, the supernatant was used to quantify the thiol-modified oligonucleotides in solution by measuring the fluorescence intensity. Sample's fluorescence emission was converted to molar concentrations by interpolation from the standard linear calibration curve.

2.7. T7-cMYC-fusion fragment amplification by Polymerase Chain Reaction (PCR)

A 252 bp fragment harboring the 23 bp T7 promoter sequence and a 229 bp fragment of the human v-myc myelocytomatosis viral oncogene homolog (MYC) gene was PCR amplified from pJET1.2 cloning vector (originally with 2974 bp; Fermentas, Vilnius, Lithuania) using the primers T7-MYCforward and MYCreverse (see Table 2.1 for sequences).

PCR amplification was performed on a MyCycler Thermocycler (Biorad) in 25 µL using 0.2 µM of each primer, 0.2 mM dNTPs, 1 U Taq DNA Polymerase (Fermentas, Vilnius, Lithuania) and 125 ng of template DNA, with the following thermal cycling conditions: intial 5 min denaturation at 95ºC, followed by 35 amplification cycles of denaturation at 95ºC for 30 s, annealing at 60ºC for 30 s, elongation at

72ºC for 30 s, and a final elongation at 72ºC for 5 min. Purification of the PCR products was performed by 1% agarose gel electrophoresis followed by excision of the respective gel band.

2.8. Inhibition of *in vitro* transcription

Standard *in vitro* transcription was performed in a volume of 50 µL containing *in vitro* transcription buffer, 10 mM of each NTP, 400 ng of the 252 bp DNA template and with 30 U of T7 RNA polymerase (Fermentas, Vilnius, Lithuania) according to the manufacturer's protocol. Reactions were incubated for 2 h at 37ºC, followed by heat inactivation of enzyme for 15 min at 75ºC.

To assess the level of inhibition by the naked oligonucleotides (T7 primer and 3T17_T7), different concentrations of each nucleotide were added to the transcription mixture. All transcription reactions were then evaluated on a 2% agarose gel electrophoresis with GelRed™ (Biotium, USA) incorporation.

Product quantity determination was performed by pixel counting using ImageJ™ imaging software. Determination of the degree of inhibition was performed after normalizing to the intensity of the positive control (100%) of the *in vitro* transcription reaction.

2.9. Inhibition of *in vitro* translation

The pGFP (4235 bp; 5Prime, GmbH, VWR International) encodes the green fluorescent protein (GFP) protein used as template for *in vitro* protein synthesis reactions. The coupled *in vitro* transcription/translation reactions were performed in a Rapid Translation System RTS 100 *E. coli* HY Kit (5Prime, GmbH, VWR International). GFP protein was synthesized for 6 h at 30ºC followed by incubation at 4ºC for 24 h for GFP maturation. GFP protein levels were measured using fluorescence spectroscopy (λ_{exc} = 395 nm, λ_{em} = 510 nm). Assessment of 3T17_RBS olignucleotide influence in translation was performed by adding 1 µg of GFP vector and crescent concentrations of the inhibitory oligonucleotide to the standard reaction mixture. The translation levels were measured as fluorescence of GFP.

3. Results and Discussion

The project comprises three major sections – Structure Design and Formation, Vectorization, and Gene Expression Silencing. Due to their modular nature in the early stages, the three sections were developed in parallel in order to avoid possible bottlenecks. The workflow assumed would also allow for the assessment of strategies initially adopted for each section and input the information gathered in the other sections, for a more efficient integration of acquired knowledge.

3.1. Structure design and formation

3.1.1. Structure design

Several criteria had to be taken into account when designing the aimed DNA structure:

- desired melting temperature
- ability of efficient gene silencing
- stability at physiologic pH and ionic conditions

To release a therapeutic DNA strand *in vivo* through thermal triggering, it is desirable that the structure's melting temperature is just above physiologic temperature. Considering that the physiologic temperature is around 37ºC, the desirable T_m range lays in the 40 to 45ºC interval. Additionally, for an efficient gene silencing, oligonucleotide strands typically with 18-25 nucleotides (Dallas and Vlassov, 2006) are employed. This would limit the sequence to adenines and timines in Watson and Crick base pairing since, for instance, a polyA of 25 nucleotides has a T_m of approximately 43ºC at low salt conditions (according to the nearest neighbor model). The use of Hoogsteen hydrogen bonds, and hence the formation of DNA triple helices, overcomes this issue as these bonds present decreased stability when compared with Watson-Crick hydrogen bonds, decreasing release temperature of the therapeutic strand. Triplex formation occurs when an oligonucleotide binds specifically to the major groove of a homopurine region of DNA. Consequently, one of the dsDNA strands has to be homopurinic so Hoogsteen bonds can be formed (Frank-Kamenetskii and Mirkin, 1995; Chan and Glazer, 1997; Duca *et al.*, 2008; Rusling *et al.*, 2009; Fox and Brown, 2011).

To achieve gene silencing *in vivo*, the structure needs to be stable at physiologic conditions prior to the therapeutic strand release. Due to their pH-independent binding to DNA, purine motifs of triplex DNA are thought to present significant stability under neutral pH (Chan and Glazer, 1997; A. Jain *et al.*, 2008). In this case, the TFO will bind in an antiparallel manner to a purine-rich strand of DNA. The use of a pyrimidine motif would require the protonation of cytosines at N3 for proper Hoogsteen bonding to N7 of guanines and therefore an acidic pH (Chan and Glazer, 1997; Duca *et al.*, 2008), non-compatible with physiologic conditions.

Previous studies suggest that the presence of divalent cations in the medium potentiate the formation of DNA triple helices due to a stability increase (Malkov *et al.*, 1993; Sugimoto *et al.*, 2001; Wu *et al.*, 2002; Wan *et al.*, 2009). The interaction of metal ions with triplexes seems not only to be

dependent on the valence of the countercations, but also on their ionic radii: in the series of Mg^{2+}, Mn^{2+}, Ca^{2+} and Ba^{2+}, the stability increases from left to right, which is in agreement with their radii ($r_{Mg^{2+}}$ = 0.66 Å, $r_{Mn^{2+}}$ = 0.80 Å; $r_{Ca^{2+}}$ = 0.99 Å, $r_{Ba^{2+}}$ = 1.34 Å), suggesting that a smaller radius may increase the stability of these structures (Sugimoto *et al.*, 2001). However, Wan *et al.* concluded that transition-metal ions Co^{2+} and Ni^{2+}, compared to alkaline-earth metal ions, show superiority in the boosting of triplex DNA formation (Wan *et al.*, 2009). They propose that this is the result of the higher affinity of transition-metal ions for purine N7 than alkaline-earth metal ions, enhancing the formation of Hoogsteen hydrogen bonds. Nonetheless, the use of free transition metals in solution is not compatible with physiologic conditions, and thus their use was discarded.

The interaction of Mg^{2+} and/or Na^{+} and triplex DNA has been thoroughly investigated (Debin *et al.*, 1999; Wan *et al.*, 2009; Lee *et al.*, 2010; Chiou *et al.*, 2011). Mg^{2+} is generally considered an enhancer of triplex formation and its main mechanism of stabilization is charge neutralization: triplex DNA has a higher charge density than that of either duplex or single stranded DNA and Mg^{2+} binds to the phosphate group, reducing the repulsion between the three phosphate frameworks. Mg^{2+} may also coordinate with N and O of bases, contributing to triplex conformation (Wan *et al.*, 2009). It has also been determined that concentrations above 10 mM do not appear to increase the stability further (Sugimoto *et al.*, 2001). Contrary to the Mg^{2+} effect, Na^{+} has been appointed as an inhibitor of the triple helix formation. The hindering effect of Na^{+} against forming triple helix DNA can be explained by polyelectrolyte effect: a high concentration of Na^{+} lowers the population of Mg^{2+} in the vicinity of DNA, lowering the population of triplex DNA (Debin *et al.*, 1999; Lee *et al.*, 2010). Na^{+} also has the ability to form undesirable dimers and tetramers, decreasing the efficiency of triplex formation even in the absence of Mg^{2+} (Lee *et al.*, 2010). Thus, on one hand, it is known that higher salt concentrations increases T_m's; on the other hand, in order to potentiate the formation of triple helices, the TFO must have a length of at least 12-14 nucleotides (Chan and Glazer, 1997), thus a balance between structure stability and desired strand release temperature must be found.

Additionally, the sequence required to form a triplex DNA structure is limited to nucleotides able to form Hoogsteen bonds, so a domain of the triplex-forming strand part has to carry the sequence that will perform the silencing. In a first stage, and to attempt to confer increased stability, this triplex-forming strand will only have 10 therapeutic nucleotides (and not the 18-25 required by literature for an efficient gene silencing).

Considering the referred limitations, the design chosen for this work is presented in Figure 3.1 and further on referred as T17, due to the 17 nucleotides forming Hoogsteen bonds present. These 17 nucleotides were chosen by taking into consideration the work of Lee and colleagues, where a similar sequence was used as the TFO (Lee *et al.*, 2010). The minor differences in sequence only diminish the probability for this sequence to form intramolecular structures.

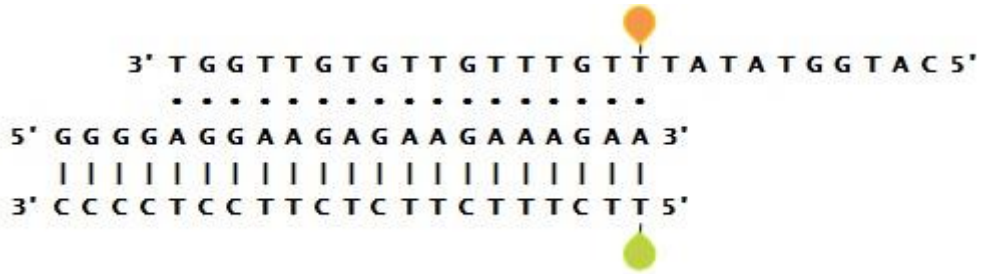

Figure 3.1 – Triplex DNA structure with 17 nucleotides forming Hoogsteen hydrogen bonds (T17 structure). Oligonucleotide designation from the top to bottom: 3T17 (or TFO); 1T17; 2T17. **|** represents Watson-Crick hydrogen bonds; • represents Hoogsteen hydrogen bonds; • represents JOE and • represents FAM. The fluorophores were only used for FRET assays and in this case the oligonucleotides labeled with JOE and FAM are referred as 3T17_11dT-JOE and 2T17_5'FAM, respectively. Every other experiment was carried out without fluorophores but the oligonucleotide sequence remained the same.

The structure presented was designed to minimize the formation of other secondary structures that might lead to malformed or unpredicted structures that could lead to incorrect analysis.

3.1.2. Structure formation assessment

Various techniques were used in order to identify and characterize the triplex DNA structure assembly. Following the characterization methods employed by others in the study of triple helix structures (Plum *et al.*, 1990; Scaria and Shafer, 1996; Lee *et al.*, 2010; Schneider *et al.*, 2010; Chiou *et al.*, 2011; Reither and Jeltsch, 2011), fluorescence and UV spectroscopy were the mainly selected techniques for the study of the T17 construct.

The formation of the T17 structure was also characterized by polyacrylamide gel electrophoresis (PAGE). However, PAGE results were not conclusive and further optimizations to this method have yet to be performed (Appendix I).

3.1.2.1. FRET analysis

FRET analysis was chosen as the main technique to assess the formation of the DNA tertiary structure and release of the TFO (the therapeutic oligonucleotide) from the double strand core.

The labeling of the structure was performed as shown in Figure 3.1. Due to the close proximity between the two fluorophores, an efficient energy transfer between the donor and acceptor dye should produce a clear variation in intensity upon triplex formation, when compared to the double-stranded structure and free TFO case. To maximize this effect, the TFO and one strand of the entrapment double helix were labeled with suitable fluorophores that form a donor/acceptor pair with high theoretical FRET efficiency and the labeling of the double strand with the donor dye was performed at the strand that does not interact directly with the TFO, while the TFO was labeled with the acceptor dye. With this arrangement, the presence of energy transfer between the fluorophore pair indicates the specific spatial proximity of the three oligonucleotides composing the T17 structure, and consequently, the formation of the triple helix structure. The theoretical FRET efficiency between the chosen

fluorophores (FAM as donor and JOE as acceptor) is approximately 95.8% (see Appendix II) for the distance predicted between the two fluorophores upon triple helix formation (Figure 2.1 and Figure 3.1). Upon melting, the triple helix is disrupted and the TFO is released from the entrapment with concomitant alteration of the spectral signal which will transduce into the increase of the donor's fluorescent emission. Control experiments employing a labeled strand with a closely related sequence, but incapable of forming a triple helix structure, were performed in order to assess the formation of unspecific secondary structures.

Taking the previously described influence of divalent and monovalent cations into account (see section 3.1.1), T17 structure formation was attempted in different binding buffers: 10 mM Tris-HCl, pH 7.6; TE 1x, pH 7.0; 10 mM sodium phosphate, pH 7.4, and discrete concentrations of $MgCl_2$ or $MnCl_2$ and/or NaCl, and the best conditions were then chosen according to the results. These experiments were carried out at 15ºC in order to maximize thermal stability for structure formation, given that the ionic requirements are met. Despite the successfulness of the referred buffers in triple helix formation in diverse studies, the above ionic conditions were all screened to determine their effect on T17 structure formation, due to its higher complexity. Sodium phosphate buffer was then excluded as a potential binding buffer after some experiments due to formation of a white precipitate at high temperature. This precipitate is likely to be magnesium phosphate, which is insoluble in water.

The experiments run in Tris-HCl (pH 7.6) and TE (pH 7) had comparable results. However, Tris-HCl was used as the binding buffer of choice for two reasons: its pH is closer to physiological pH and also, the presence of EDTA (a powerful chelating agent that binds Mg^{2+} ions with high association constant) in TE competes with the triple helix for the magnesium in solution introducing solution equilibrium considerations that unnecessarily complicates the analysis.

Figure 3.2 shows the emission spectra of samples in the presence of the three oligonucleotides (1T17, 2T17_5'FAM and 3T17_11dT-JOE), in different concentrations of $MgCl_2$ and/or NaCl.

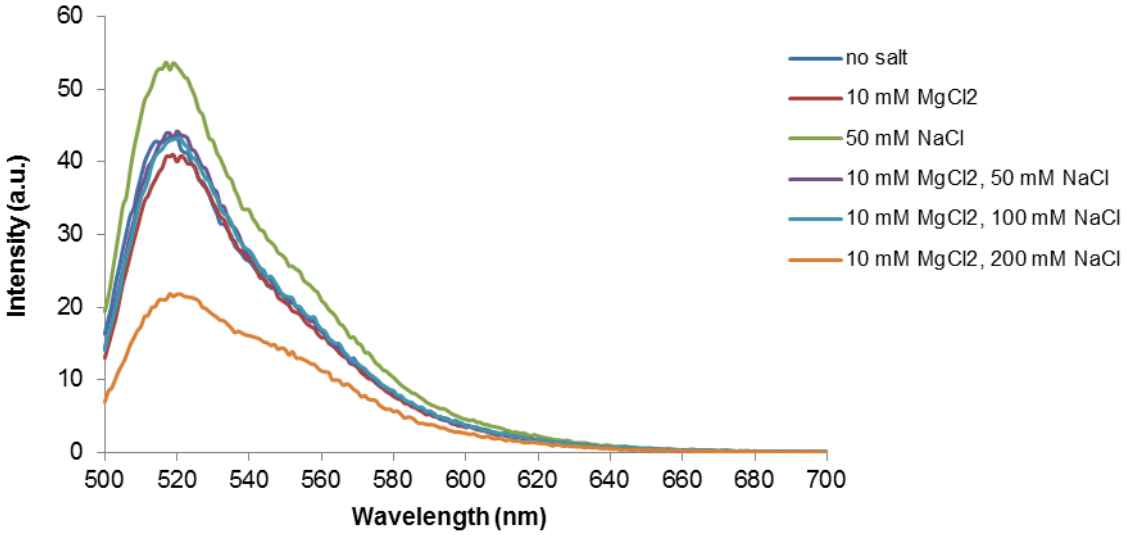

Figure 3.2 – Emission spectra (λ_{exc} = 490 nm) of structure T17 in 10 mM Tris-HCl (pH 7.6) and different concentration of $MgCl_2$ and/or NaCl at 15ºC. Besides a peak at 520 nm, JOE emission at 550 nm is visible in every ionic condition tested; this is a result of JOE direct excitation at 490 nm.

Results show the donor emission peak at 520 nm and the emission of JOE (with maximum at 550 nm), even in the absence of Mg^{2+} and Na^{+}. The presence of JOE emission in all the saline conditions assayed does not directly indicate triple helix formation, since a strong JOE direct excitation component is present when the solution is excited at 490 nm (see Figure 2.1). In the absence of stabilizing ions (Mg^{2+}) or when JOE is functionalized to a non-TFO oligonucleotide, emission of the acceptor is systematically present in the measured emission spectra (see Appendix III, Figure A.2), corroborating that the presence of JOE emission does not unequivocally indicate T17 structure formation. The decrease of both donor and acceptor emission for the highest salt concentration, when compared to the other samples, is due to the quenching effect of chloride, the counterion used for both sodium and magnesium salts.

FAM and JOE are both fluorescein derivatives which present strong spectral overlap. On one hand, the high overlap between FAM emission and JOE absorption allows for very efficient energy transfer yields; on the other hand, the overlapping absorption of both fluorophores (at 490 nm, the absorption by FAM is 78000 $M^{-1}cm^{-1}$ and by JOE is approximately 28630 $M^{-1}cm^{-1}$; Figure 2.1), makes this FRET pair a less-than-ideal choice. However, this pair was selected as a consequence of two intrinsic limitations of the system:

1) The triplex structure is to be functionalized onto the AuNPs' surface in a posterior phase, where the melting of the triple helix has to be followed by FRET analysis, in a parallel approach as free-DNA studies. Previous results in our group succeeded to demonstrate that rhodamine derivative compounds interact irreversibly with the AuNPs' surface through the amine groups. This observation discards the choice of rhodamine-like acceptors that might be a better fit for FRET pairs.

2) The AuNPs chosen have a plasmon resonance absorption in the 520 nm region, so in order to prevent possible intern filter effects due to the nanoparticle presence, the fluorophore choice was further limited to fluorescein derivatives.

Additionally, due to budget constraints it was necessary to choose a FRET pair that suited both the free DNA analysis and its posterior utilization in the presence of AuNPs.

The considerable contribution of direct excitation of JOE rendered challenging the splitting of the contribution of FRET and direct excitation to the overall measured emission. To overcome this problem, excitation spectra were measured instead. An excitation spectrum measures the fluorescence intensity at a single emission wavelength, upon scanning of the excitation wavelengths. In practical terms, it will give the relative weight of energy transfer and direct excitation at 550 nm when compared to the absorption spectrum of the sample. The emission wavelength has to be carefully chosen to minimize donor's emission. It should be noted that due to the strong spectral overlap of the two dyes, a complete splitting of both processes is not possible using steady-state fluorescence techniques. For a better understanding of the analysis performed and the relevance of excitation spectra to this situation refer to Appendix IV, which shows the different outcomes when measuring the excitation spectra of samples with different combinations of fluorophores.

Here, the emission wavelength was set at 640 nm where FAM emission is considerably smaller than JOE's (Figure 2.1). Figure 3.3 shows the comparison between the absorption spectrum of the T17 structure-forming oligonucleotides in 10 mM Tris-HCl and excitation spectra at different concentrations of $MgCl_2$ and/or NaCl.

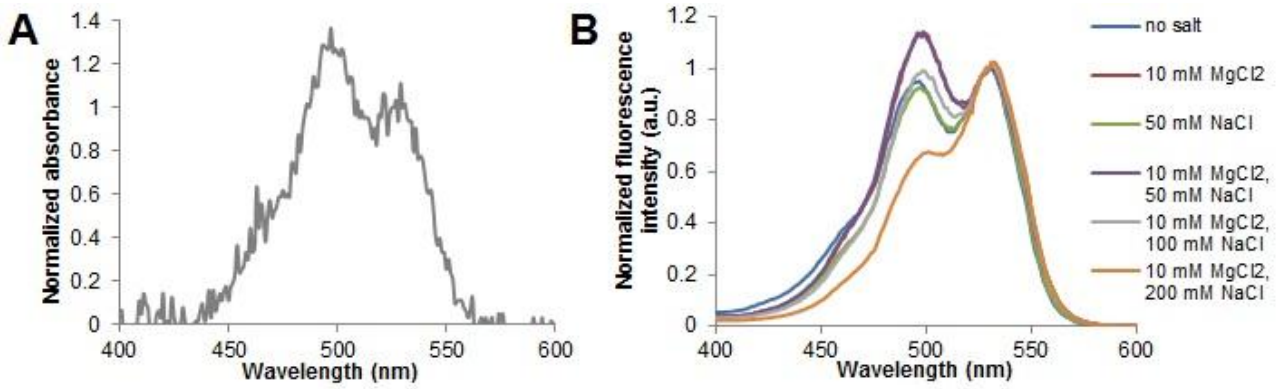

Figure 3.3 – T17 structure formation assessment by comparison between A) absorption spectrum of the mixture and **B)** excitation spectra (λ_{em} = 640 nm) at different concentrations of $MgCl_2$ and/or NaCl. In the excitation spectra, there is a clear inversion of the peaks in 10 mM $MgCl_2$ and 10 mM $MgCl_2$, 50 mM NaCl which might indicate the T17 structure formation.

Results show that saline conditions lead to different fluorescence intensities at 490 nm. According to previous studies, high sodium concentration deters the formation of triple helices, and thus, at a concentration of 200 mM of NaCl, no triplex formation was expected (Figure 3.3B – orange series). It can be seen that at this salt concentration some emission was obtained through excitation at 490 nm which is solely due to FAM direct emission. Additionally, measurements where a closely related

oligonucleotide that is unable to form triple helices is used yield similar results (Appendix III, Figure A.3). For the other salt conditions tested, they all present increased emission at 490 nm excitation. This increase is due to energy transfer from FAM present in the double helix motif to the JOE located in the TFO strand, indicating the presence of a triple helix structure. Higher yields of triple helix formation were attained when 10 mM $MgCl_2$ and 10 mM $MgCl_2$ plus 50 mM NaCl were used. These observations are in accordance with previous reports (Lee *et al.*, 2010). Curiously, the presence of 50 mM NaCl when 10 mM $MgCl_2$ is also present in solution does not evidence destabilization of the structure, even though it was expected that this Na^+ concentration would decrease T17 structure yield. Due to the considerable contribution of direct FAM emission in the excitation spectra, only qualitative results can be given, and no accurate yields on the T17 structure formation can be obtained.

The condition chosen to perform further characterization of the T17 structure was 10 mM $MgCl_2$.

Similar ionic conditions were used with $MnCl_2$ as an enhancer for the formation of the construct and results comparable to those using $MgCl_2$ were obtained (Figure 3.4). It can be observed that FAM's emission peak diminishes when in the presence of Mn^{2+}. However, that decrease in the donor's fluorescence intensity is not accompanied by an increase in the acceptor's intensity, which would demonstrate an energy transfer process. In can also be observed that the emission peak of FAM is more intense when NaCl is present in solution and that intensity increases with the increase of NaCl concentration. The donor's intensity peak reaches its maximum intensity in this assay when the divalent cation is not present in solution. This is in agreement with the literature (Lee *et al.*, 2010) as Na^+ is an inhibitor of triple helix formation. Due to time constrains, the work with this salt was discontinued.

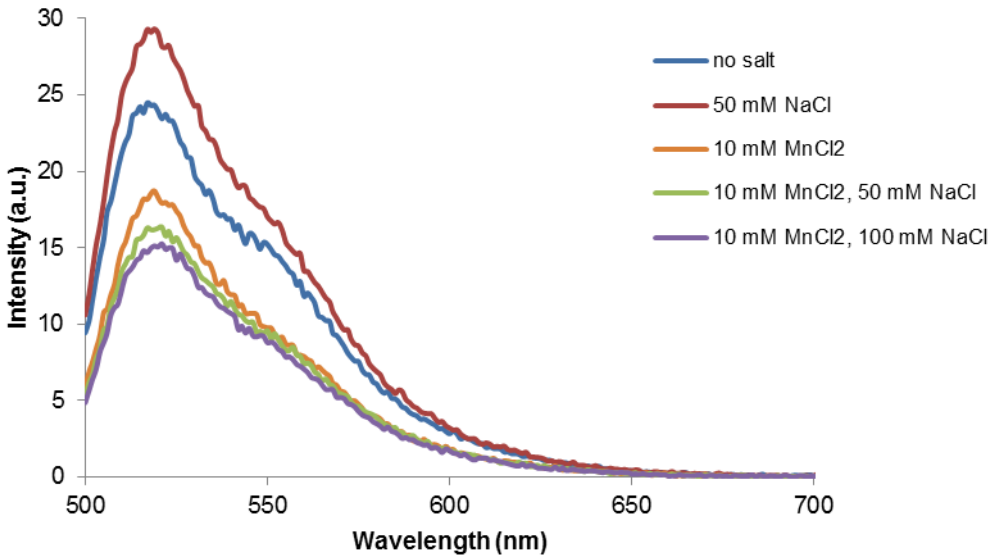

Figure 3.4 – Emission spectra (λ_{exc} = 490 nm) of structure T17 in 10 mM Tris-HCl (pH 7.6) and different concentration of $MnCl_2$ and/or NaCl at 15ºC. Besides a peak at 520 nm, JOE emission at 550 nm is visible in every ionic condition tested; this is a result of JOE direct excitation at 490 nm. These results are comparable to those in Figure 3.2.

3.1.2.2. Melting profiles

In order to compare the results obtained by FRET to a standard technique in the analysis of the nucleic acids structure, UV melting curves were measured. Figure 3.5 shows the melting curves of the T17 structure-forming oligonucleotides, the double helix without the TFO, and the double helix oligonucleotides with a non-TFO control of triplex formation.

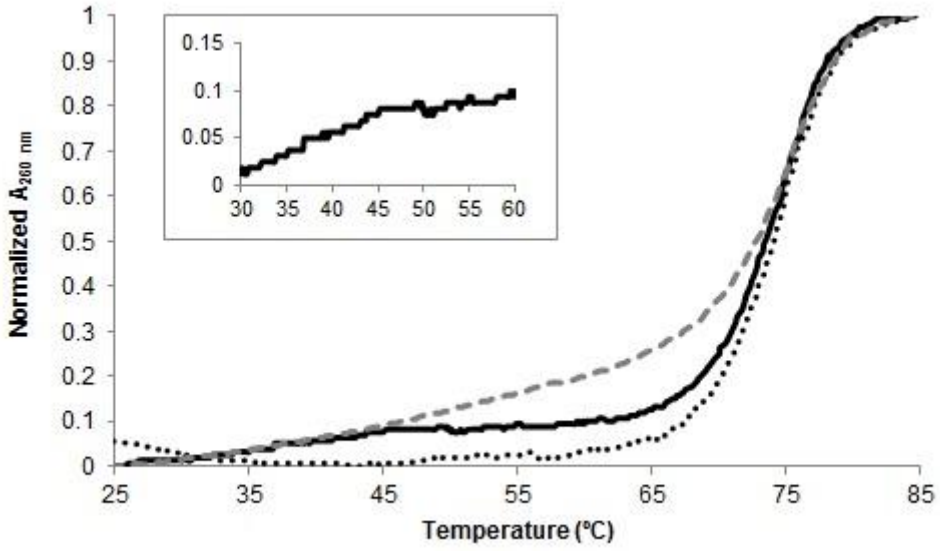

Figure 3.5 – Melting profiles followed by absorption at 260 nm in 10 mM Tris-HCl and 10 mM $MgCl_2$. Black solid line: T17 structure-forming oligonucleotides (1T17, 2T17 and 3T17); black dotted line: T17 double helix (1T17 and 2T17); grey dashed line: T17 double helix (1T17 and 2T17) and non-TFO. The inset highlights the transition from triplex structure to double helix and 3T17 oligonucleotide that occurs around 40ºC.

Results show that when the T17 double helix is present, only one sharp transition at approximately 75ºC is observed. This value is in agreement with the predicted temperature according to the nearest neighbor model (circa 81ºC) for this saline condition. When the triple-helix forming oligonucleotide is present, a second transition is observed at around 40ºC, indicating the dissociation of a less stable structure. Assuming the presence of the triple helix construct, and according to DNA hyperchromicity theory, one would expect Hoogsteen hydrogen bonds to be less stable than typical Watson-Crick ones, although triple helix formation induces further tighter stacking within the tertiary structure domain, decreasing structure absorbance. Moreover, by design only 17 bases forming Hoogsteen bonds are predicted versus 21 bases forming Watson-Crick bonds present forming the double-stranded component. Seventeen bases forming Hoogsteen bonds correspond to 34 hydrogen bonds (see Figure 1.3) that are less stable than their Watson-Crick counterparts. These Watson-Crick hydrogen bonds are also present in higher number – 52 in total. The overall result should be a more subtle transition than the one found in simple double helix dissociation, and at lower temperatures. These results are thus in agreement with the dissociation profile expected from a triple-helix structure. At the ionic strength used in this assay, the T_m of the triplex transition is around 40ºC which would allow the structure to remain fairly stable at physiological conditions (approximately 37ºC). Inside the cells, the structure would respond to the mild temperature raise by laser irradiation at considerably

lower energies than required to melt a double strand, resulting in less healthy tissue damage. Temperature is a function of the distance from the center of the nanoparticle and is related to the incident energy of irradiation (Govorov *et al.*, 2006; Govorov and Richardson, 2007). Therefore, although the triplex fraction of the structure is more distant from the center of the nanoparticle, the temperature increase needed to melt is lower and consequently, the energy and/or time of irradiation should be lower than to melt the double strand fraction.

Also represented in Figure 3.5 is the melting curve of the double helix in T17 structure and a non-TFO. This control melting curve permits to identify artifacts in the triplex transition due to the possible presence of non-specific secondary/tertiary structures. This oligonucleotide is not able in principle to form neither triplex nor duplex structures with any of the other two oligonucleotides. The melting curve shows, however, from 0 to 45ºC, a profile that coincides with T17 melting curve. But the absorbance continues to increase linearly until it reaches roughly 65ºC and after that, a clear sigmoidal fraction of the curve appears, regarding dsDNA to ssDNA transition. Control melting curves of each oligonucleotide used alone show that the increase in the absorbance until 65ºC is due to intramolecular interactions, that are only formed in the absence of more thermodynamically stable structures. In the presence of 1T17 and 2T17, 3T17 yields a different melting profile than compared when it is the only oligonucleotide in solution. The transition at 40ºC is only observed when all three T17 forming oligonucleotides are present. This taken together with the FRET experiment results corroborates that, indeed, the transition obtained is due to the release of the TFO strand from its duplex scaffold.

3.2. Vectorization

AuNPs were used as vectors to the DNA delivery, as shown in Figure 3.6A. Unfortunately, due to time constrains, the first step of the conjugates characterization and development involved exclusively the double helix of the T17 structure conjugated with AuNPs as depicted in Figure 3.6B.

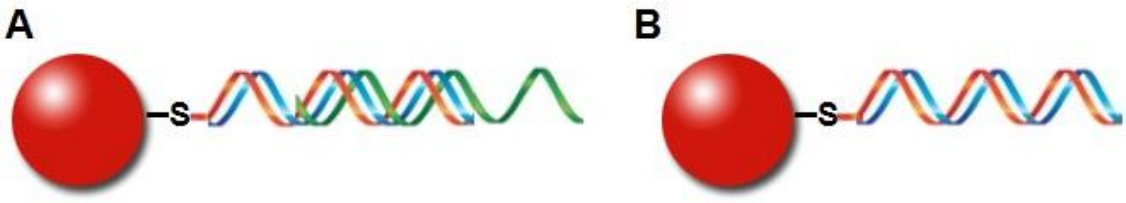

Figure 3.6 – Scheme of AuNP conjugates. A) AuNP conjugated with the complete T17 structure; **B)** AuNP conjugated with the double strand of T17 structure. For oligonucleotide sequences refer to Figure 3.1. AuNPs are functionalized via thiol group of one of the oligonucleotides. For clarity, one structure is represented per AuNP but note that AuNPs will be functionalized with more than one DNA structure.

3.2.1. DNA-AuNP conjugates synthesis and characterization

Spherical AuNPs with a diameter of 14 nm were synthesized via the citrate reduction method as previously described (Lee and Meisel, 1982). The average size and morphology of the particles was determined by TEM – see Appendix V.

Previous results showed that when AuNPs are functionalized with single-stranded DNA, and in the presence of free complimentary oligonucleotides, only a small fraction of the AuNP-probes hybridize with its complementary target. Thus, the functionalization strategy adopted involved direct functionalization of previously hybridized dsDNA. Contrary to the functionalization of ssDNA in which an optimized protocol to achieve maximum loading is already available in the literature (Hurst *et al.*, 2006), the best method to directly functionalize dsDNA to AuNPs or the way to obtain a 1:1 stoichiometry of the strands is not established so far. The AuNPs were functionalized with pre-hybridized dsDNA, in which only one of the strands is modified with a thiol group at the 5' end (Figure 3.6B). Different approaches were followed in order to find the best conditions (Table 3.1). Both oligonucleotides (1T17_5'thiol_3'FAM and 2T17_5'JOE) are labeled with a fluorophore at the 5' or 3' end (see Table 2.1), and the melting curve of the dsDNA should be followed by FRET analysis between this pair in order to determine the T_m of the double strand.

Table 3.1 – Summary of the methods attempted for dsDNA functionalization to AuNPs.

Method #	Capping molecule	Method protocol	Ratio AuNP:dsDNA
1	Citrate	Functionalization adapted from Hurst *et al.*, 2006; salt-aging process until 0.3 M NaCl.	1:100
2		Incubation of dsDNA with AuNPs for 48 hours (without salt addition).	
3		PEGylation of AuNPs in various concentrations followed by dsDNA functionalization to PEG-AuNPs and salt-aging process until 0.3 M NaCl.	1:200
4	Phosphine	Functionalization adapted from Hurst *et al.*, 2006; salt-aging process until 0.3 M NaCl.	
5	Citrate	Functionalization adapted from Hurst *et al.*, 2006; salt-aging process until 0.2 M NaCl.	

Method #1 is an adaptation of the protocol already optimized to ssDNA (Hurst *et al.*, 2006) and led to aggregation of the AuNPs. This method involves a salt-aging process where the ionic strength is increased gradually with time. This ensures that the charge of the ssDNA backbone is shielded, allowing the approximation between ssDNA and AuNPs (negatively charged due to its citrate capping). Also, this method includes sonication between salt additions, avoiding unspecific adsorption of the oligonucleotides onto the AuNPs' surface. The salt-induced aggregation that happened when using this protocol to conjugate dsDNA occurred probably because, when in double strand, the functionalization does not follow the same kinetic rate as ssDNA. The dsDNA is likely to require higher salt to achieve stabilization; however, the AuNPs do not and the charge neutralization induced by the increase of ionic strength makes them to come closer, leading to aggregation of the AuNPs.

Method #2 maintained the mixture red after 48 hours, indicating that AuNPs kept their disperse form. The visible absorption maximum of the conjugates was only 2 nm red-shifted from the non-functionalized AuNPs' solution, indicating poor functionalization. Indeed, when emission spectra were measured, the emission of FAM and JOE were not detected. To determine if the functionalization was effective, displacement of the thiol groups binding was performed by adding DTT to the medium as described in section 2.6. Fluorescence present in the supernatant indicates that the thiol-modified oligonucleotide was functionalized onto the AuNPs' surface. However, DTT was not able to displace every thiol group from the surface of the nanoparticles as the solution still remained red. β-mercaptoethanol was used instead, yielding better results. Thus, the absence of fluorescence might be explained by nonspecific adsorption of DNA to the AuNPs' surface due to DNA's negatively charged backbone.

In order to prevent nonspecific adsorption, another approach was pursued: addition of polyethylene glycol (PEG) to the AuNPs surface (Method #3). PEGs are expected to stabilize the AuNPs – allowing for the use of a salt-aging procedure – and to block the nonspecific adsorption of DNA to the AuNPs' surface and interspace the dsDNA molecules. Additionally, the presence of this molecule decreases the probability of cross-talk between the fluorophores from different dsDNA molecules. Moreover, this molecule would further stabilize the dsDNA-AuNPs and favor the uptake by cells (Liu *et al.*, 2007) which will be utterly important when this system is to be applied *in vivo*. Different concentrations of PEG were screened to determine the optimal concentration for the stabilization of AuNPs (favored with higher concentrations of PEG) versus loading of oligonucleotides onto the AuNPs' surface and fluorescent signal strength (favored with lower concentrations of PEG). The minimal concentration of PEG which maintained the SPR around 520 nm was 0.006 mg/mL (Appendix VI). At lower concentrations of PEG, the absorption maximum is red-shifted, indicating aggregation of the nanoparticles. Only the PEG-AuNPs conjugates that did not present aggregation were used to the dsDNA functionalization. PEG-AuNPs were then functionalized with previously hybridized dsDNA and did not suffer aggregation during salt-aging process. This approach turned out to be ineffective – the emission spectrum showed no emission of FAM and/or JOE, and additional studies are required to assess the AuNPs' functionalization efficiency.

The change of capping molecule in method #4 would allow following a regular synthesis without the concern of aggregation during the salt-aging process because this capping renders assembly and disassembly of AuNPs reversible (Han *et al.*, 2008). Despite having assembled during the salt-aging process, the synthesis was resumed and the conjugate solution turned red after a brief centrifugation and change of the supernatant to a 25% (w/v) phosphine solution.

The emission spectrum obtained showed emission at 520 nm, indicating the presence of FAM-labeled oligonucleotide. At room temperature and considering the structure shown in Figure 3.6B, JOE's emission should be observed preferably instead. Surprisingly, a day after synthesis it was not possible to detect neither FAM's emission nor JOE's emission. Instead, one peak at 585 nm was visible which was concluded to correspond to the Raman peak of water. It was observable when the

conjugates were analyzed because there is no emission of other molecules and therefore its peak became significant in the spectrum. There are two possible explanations for these results:

1) Immediately after synthesis, the FAM-labeled oligonucleotide was present free in solution or with low loading yield, or;
2) An interaction between phosphine and the fluorophores (both are fluoresceins derivatives) that follows a slow kinetics leads to fluorescein degradation.

The second hypothesis was discarded after measuring the emission of FAM (not bonded to an oligonucleotide, i.e., in its free form) in a 25% (w/v) phosphine solution and its fluorescence did not quench. However, due to time constrains, this approach had to be abandoned.

Analyzing the previous attempts using citrate as capping agent of the AuNPs, several conclusions can be drawn:

1) The simple addition of dsDNA previously hybridized to a colloidal solution of AuNPs leads to poor functionalization and no fluorescence signal could be obtained;
2) Following the salt-aging process described elsewhere (Hurst *et al.*, 2006) with dsDNA results in AuNPs' aggregation at low salt concentrations.

Method #5 reached the compromise regarding these two procedures: less functionalization than if the synthesis was completed for the ssDNA case, but higher than the simple addition of dsDNA to AuNPs; and no aggregation of the AuNPs should be verified. The solution remained red during the synthesis and when emission spectra were measured, a peak at approximately 520 nm was detected, corresponding to emission of FAM but there was no peak at 550 nm that would correspond to JOE's emission (Figure 3.7).

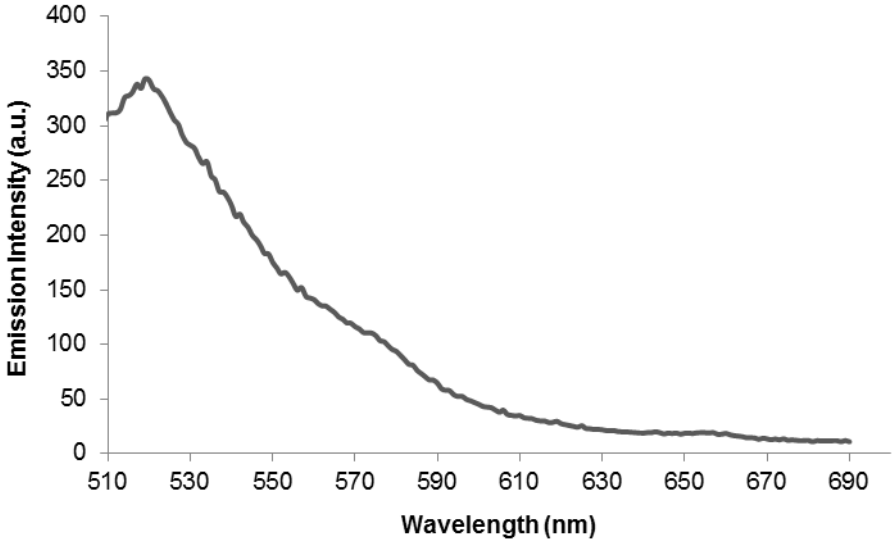

Figure 3.7 – Emission spectrum of the dsDNA-AuNP conjugates measured at an excitation wavelength of 490 nm and at 20ºC. The peak observed at approximately 520 nm corresponds to emission of FAM and emission at 550 nm (corresponding to JOE) is not observable.

The lack of emission at 550 nm in Figure 3.7 indicates that no energy transfer occurred. Most likely, this was due to the absence of hybridization between the JOE-labeled strand and its FAM-labeled counterpart. The theoretical T_m of the two oligonucleotides functionalized onto the AuNPs' surface (1T17_5'thiol_3'FAM and 2T17_5'JOE) is approximately 52ºC, thus, it is unlikely that the absence of JOE emission is due to thermal denaturation. Poor double strand functionalization could explain this result even though the two oligonucleotides were hybridized previously to conjugation with the particles. Another explanation for this observation may be a high yield formation of double stranded construct but due to the great proximity between the two fluorophores, the presence of an electron transfer or other non-radiative deactivating process may lead to JOE quenching. Since the FAM quantum yield is considerably higher than JOE's (0.95 vs. 0.75), FAM emission would still be observed. Thus, to understand which hypothesis is most likely to be correct, evaluation of the functionalization effectiveness of thiolated strands and of dsDNA onto AuNPs' surface was performed by two sequential assays:

1) Assessment of dsDNA functionalization by chemical denaturation of dsDNA with NaOH;
2) Determination of thiol-functionalized oligonucleotides with β-mercaptoethanol.

The first test is based on the disruption of the hydrogen bonds between DNA strands by a strong alkaline pH (pH = 13), leading to the release of 2T17_5'JOE oligonucleotides from the vicinity of the AuNPs. Since this strand is not directly attached to the nanoparticles, after denaturation it stays in the supernatant. The measurement of fluorescence intensity of the supernatant allows the quantification of the amount of dsDNA present in that concentration of AuNPs and therefore estimate the number of dsDNA functionalized to each AuNP. The concentration of 2T17_5'JOE present in the samples was 0.006 ± 0.001 μM (see Appendix VII for the quantification results) which corresponds to a yield of 0.5% – Table 3.2. The second test is based on the cleavage of thiol groups from the AuNPs' surface using a reducing agent (DTT or β-mercaptoethanol). Here, β-mercaptoethanol was the reducing agent of choice given the previous poor results with DTT. The thiolated oligonucleotide is labeled at the other end with a fluorophore (FAM) which allows the quantification of functionalized strands by measuring the supernatant fluorescence after oligonucleotide detachment from the AuNPs. The concentration of 1T17_5'thiol_3'FAM present in the samples was 0.706 ± 0.024 μM (see Appendix VIII for the quantification results) and that represents a 70.1% yield – Table 3.2.

Table 3.2 - Quantification of AuNPs' surface functionalized oligonucleotides.

	Oligonucleotides per AuNP (pmol/cm^2)	**Strands per AuNP**	**Yield (%)**
2T17_5'JOE	0.32 ± 0.05	1	0.5
1T17_5'thiol_3'FAM	38.2 ± 1.3	140.2	70.1

Poor functionalization in double strand is therefore the cause of the lack of JOE's emission in Figure 3.7. With 1 strand of JOE-labeled oligonucleotide to 140 strands of FAM-labeled oligonucleotide per AuNP, and taking into account the higher quantum yield of FAM, JOE's emission could not be perceived in the emission spectrum. Considering that the oligonucleotides were

hybridized prior to functionalization with the particles, this stoichiometry should be approximately 1:1. This disparity could have been caused by sonication during synthesis. Ultrasounds in aqueous solution generate cavitation bubbles and these can cause damage to nucleic acids by means of mechanical or thermal degradation (Elsner and Lindblad, 1989; Larguinho *et al.*, 2010). Although fragmentation of DNA is not a concern in this case because its length is not long enough to be cleaved by this process, thermal degradation destroys dsDNA. Despite staying in solution, the denatured oligonucleotides might not be able to re-hybridize with the tiolated complementary DNA bound to the AuNPs due to steric hindrance because more thiolated oligonucleotides are loaded in the meantime. To avoid this issue, sonication should be circumvented. Also, both oligonucleotides should be thiolated in order to potentiate the stabilization of dsDNA conjugated with the AuNPs and attain a stoichiometry closer to 1:1.

Despite this disparity which impairs the determination of the dsDNA-AuNPs' T_m by FRET melting analysis, this parameter was determined in a two-step assay:

1) Chemical denaturation profile of the double helix from the dsDNA-AuNP conjugates with NaOH through increments of pH;
2) Determination of T_m of the dsDNA without the AuNPs by absorbance at 260 nm in the same ionic conditions (10 mM sodium phosphate buffer, pH 8.0).

The melting curves were then overlapped to associate a pH to a temperature and determine the T_m in these conditions and the results are represented in Figure 3.8.

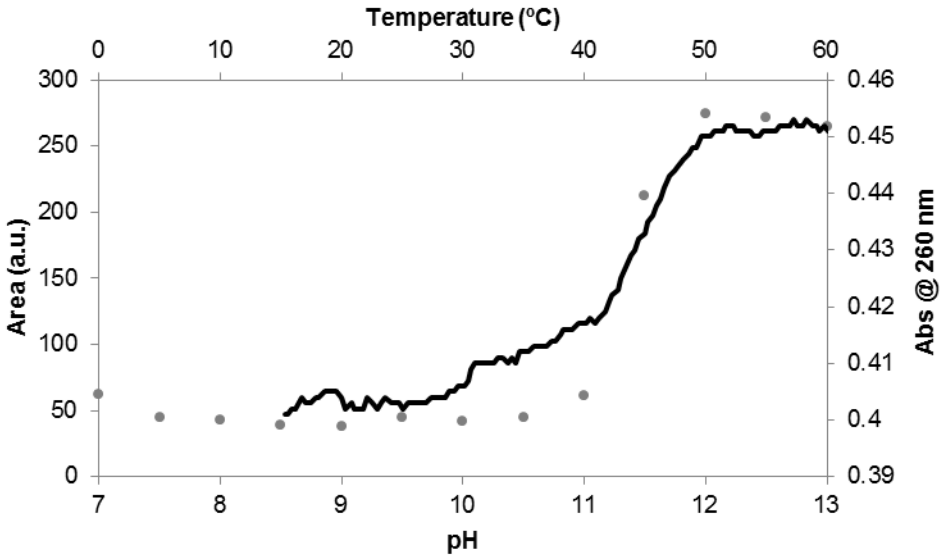

Figure 3.8 – Double helix of T17 structure conjugated to AuNPs melting temperature determination by the area of fluorescence intensity spectra of 2T17_5'JOE at increasing pH (grey dots) and by absorbance at 260 nm of the double helix (black line) in 10 mM sodium phosphate buffer (pH 8.0). The T_m according to the UV melting curve is approximately 44ºC which corresponds to a pH around 11.3.

The melting transition of dsDNA-AuNPs is around pH 11.3 which corresponds to a temperature of roughly 44ºC. This temperature is lower than the previously determined but one has to bear in mind that no salt was present in both samples and that decreases the stability, the energy required to

disrupt the hydrogen bonds is inferior and thus transitions occur at lower temperatures. And it is actually in agreement with the theoretical T_m at this salt condition (approximately 40ºC according to the nearest neighbor method). It would be valuable to repeat this assay in T17 structure formation conditions in order to have a more reliable analysis for the fully operational system.

3.2.2. Triple stranded DNA (tsDNA)-AuNPs formation assessment

Gel electrophoresis has proved effective in the differentiation between ssDNA-AuNPs and dsDNA-AuNPs (Pellegrino *et al.*, 2007) based on surface charge of AuNPs. Following the same principle, tsDNA-AuNPs should migrate less that dsDNA-AuNPs due to its higher total molecular weight.

Three samples with a concentration of 25 nM were prepared in 10 mM Tris-HCl (pH 7.6) and 10 mM $MgCl_2$: ssDNA-AuNP, dsDNA-AuNPs and tsDNA-AuNPs. The first was obtained by denaturing the dsDNA-AuNPs with NaOH and discard of the supernatant; and the third one was obtained by hybridizing 3T17 oligonucleotide with dsDNA-AuNPs. The conjugates' stability in these conditions was previously tested with positive results. The resulting gel did not show a different migration pattern for any of the conjugates (Figure 3.9). This can be easily explained by the ineffectiveness to form high yield dsDNA-AuNPs conjugates as already demonstrated in Table 3.2. Nonetheless, the lack of differential migration between dsDNA-AuNPs and tsDNA-AuNPs is the result of poor Hoogsteen hydrogen bonds formation. This might have occurred due to the high yield loading of AuNPs with ssDNA, preventing the approximation of 3T17 oligonucleotide.

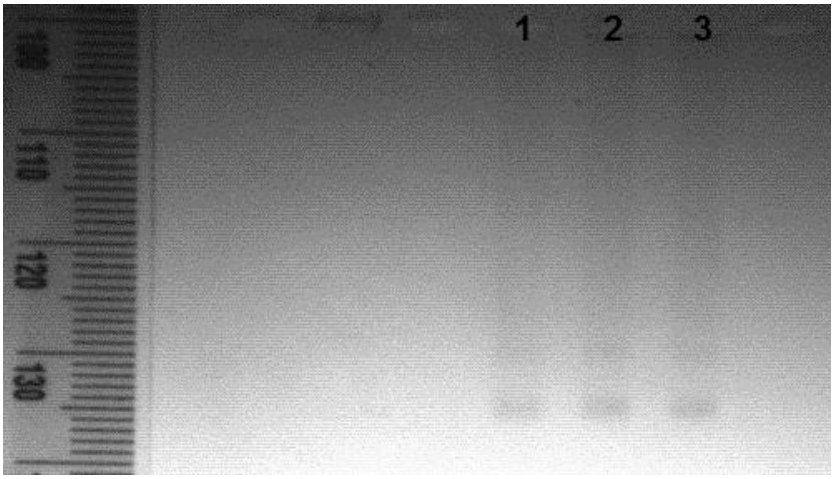

Figure 3.9 – Electrophoretic analysis of conjugates in 1% agarose. Conditions: 2 hours at 6 V/cm in 1x TBE buffer. Lanes: 1- ssDNA-AuNPs; 2- dsDNA-AuNPs; 3- tsDNA-AuNPs. The lack of differential migration denotes the lack of functionalization both in dsDNA and tsDNA of AuNPs. If AuNPs were functionalized with dsDNA and tsDNA in lanes 2 and 3 respectively, lane 1 should show the fastest migration due to lower surface charge and lane 3 the slowest due to high surface charge.

3.2.3. Theoretical calculation of laser intensity to triple strand delivery from AuNPs

Although not fully developed yet, this system of vectorization will in principle allow specific delivering of the third strand (3T17 oligonucleotide) due to the capability of AuNPs to generate heat upon irradiation with a laser of frequency overlapping the SPR peak (Sperling *et al.*, 2008). Lasers

with a frequency of 532 nm are the most common for applications with metal nanoparticles so that is the frequency used to calculate the laser intensity. The temperature increase is a function of the distance from AuNPs' surface (Govorov *et al.*, 2006; Govorov and Richardson, 2007) and therefore is necessary to take that factor into account – in this case the distance is of circa 8.3 nm to the end of the Hoogsteen bonds formed by 3T17 oligonucleotide. The temperature increase required to release the third strand is 3ºC, considering that the T_m obtained by UV melting curve (40ºC) is accurate and the physiologic temperature is 37ºC.

According to Govorov and colleagues (Govorov *et al.*, 2006; Govorov and Richardson, 2007), the intensity of the laser had to be at least $3.0x10^5$ W/cm^2 (see Appendix IX for the complete calculation).

3.3. Silencing gene expression

The final objective proposed for this work was to achieve an efficient silencing of a malignant gene by means of inhibiting its transcription or, and preferably, its translation into a protein.

3.3.1. Inhibition of *in vitro* transcription via antisense DNA

Due to simplicity of the process, inhibition of *in vitro* transcription was attempted first using two antisense oligonucleotides (antisense T7 and 3T17_T7; *vide* Table 2.1 for sequences): antisense T7 consists of 23 nucleotides complementary to those of the sense strand of the promoter region recognized by T7 RNA Polymerase; and 3T17_T7 is an oligonucleotide containing the 17 triplex forming nucleotides of the T17 structure at downstream and the antisense of the T7 promoter at upstream. For a more comprehensive view, see Figure 3.10.

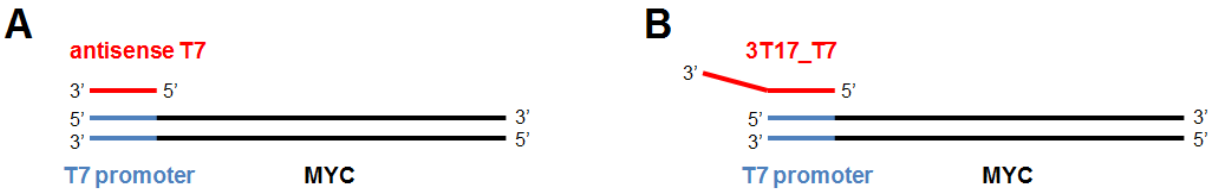

Figure 3.10 – Strategy for silencing gene expression using antisense oligonucleotides. A) Using an oligonucleotide 100% complementary to the sense strand of T7 promoter region (antisense T7). **B)** Using an oligonucleotide with a TFO at downstream and 23 nucleotides complementary to the sense strand of T7 promoter (3T17_T7).

The T7 promoter antisense oligonucleotide has already proved to successfully inhibit the *in vitro* transcription (Conde *et al.*, 2010). As proof of concept, a fragment of MYC was used as template for inhibition. The protein encoded by this gene is a nuclear phosphoprotein (Kato and Dang, 1992). MYC does not act solely as a classic transcription factor as it can also globally influence chromatin structure and affect genetic programs, namely cell cycle progression, apoptosis and differentiation. Mutations, overexpression, chromosomal translocation and gene amplification of this gene were shown to

promote a spectrum of malignancies, including tumors, leukemias and lymphomas (Wasylishen and Penn, 2010).

In an attempt to simulate what would happen when the system of antisense delivery was applied to cells, a simplified system was tested where increasing concentrations of the inhibiting oligonucleotide were added to a fixed concentration of template DNA without previous hybridization of both sequences. Figure 3.11 shows the comparison between the effectiveness of oligonucleotides antisense T7 and 3T17_T7 to block the transcription machinery by hindrance of the promoter site.

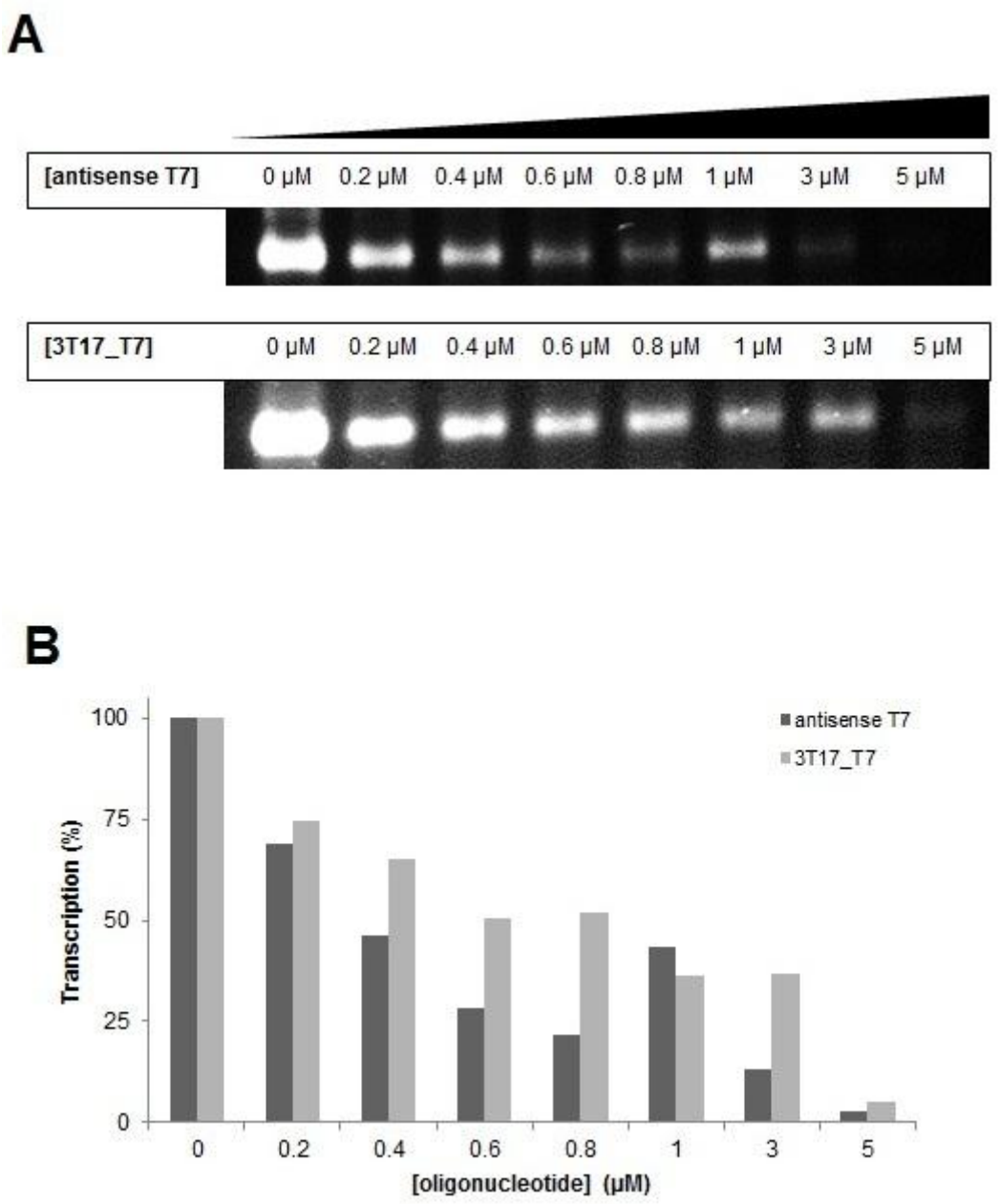

Figure 3.11 – Inhibition of *in vitro* transcription via antisense oligonucleotides. A) Agarose gel electrophoresis of *in vitro* transcription reactions in the presence of increasing 3T17_T7 oligonucleotide concentration. The represented bands correspond to the mRNA product produced by *in vitro* transcription. **B)** Transcription levels as function of increasing concentration of the inhibitory oligonucleotide (antisense T7 or 3T17_T7). Determination of the degree of inhibition was performed after normalizing to the intensity of the positive control (100%) of the *in vitro* transcription reaction. DNA template band was used as internal standard to minimize illumination and gel loading heterogeneities.

As it can be observed, increasing antisense oligonucleotide concentration leads to a decrease in transcription product up to approximately 10% of its native levels. Antisense T7 oligonucleotide was proven more effective in inhibiting *in vitro* transcription than 3T17_T7 oligonucleotide (Figure 3.11B). This was the expected result considering that antisense T7 is 100% complementary to the T7 promoter region and 3T17_T7 has a non-complementary portion (TFO portion) that possibly destabilizes the hybridization with the promoter. Nonetheless, 3T17_T7 is clearly able to prevent enzymatic activity (Figure 3.11A) with comparable efficiencies. The concentration of DNA template in each transcription reaction was of approximately 3 µM. It was thus expected that at least a 3 µM concentration or, most likely, an excess of inhibitory oligonucleotide would be needed to completely suppress *in vitro* transcription. When 3 µM of antisense T7 or 3T17_T7 is added, the percentage of transcription is of only 13% and 37% respectively and 3% and 5% respectively with 5 µM of inhibitory oligonucleotide in the medium (Figure 3.11B). The T7 RNA polymerase is highly specific for its individual promoter sequence and transcription will only occur in DNA sequences harboring the T7 promoter region (Rong *et al.*, 1998; Durniak *et al.*, 2008). Hybridization of these inhibitory oligonucleotides to the promoter sequence hinders this region, impairing the recognition by the polymerase and consequently, the transcription of the downstream sequence.

Besides lowering the level of *in vitro* transcription, the addition of these oligonucleotides in the reaction had an additional effect: several bands with lower molecular weights than the mRNA product are also visible in the gel (see Appendix X, Figure A.10). When transcription begins, i.e. when the polymerase recognizes its promoter, it unwinds the template DNA due to its helicase activity (Yin and Steitz, 2002; Yin and Steitz, 2004) and the inhibitory oligonucleotide might hybridize with its complementary sequence, which could cause the polymerase to halt transcription and therefore, produce shorter fragments of RNA. In order to evaluate the likelihood of this, transcription reactions where the inhibitory oligonucleotide and template DNA were previously hybridized were performed. This experiment would eliminate the vast majority of the abortive transcriptions although not completely due to the higher thermodynamic favorability towards hybridizing both strands of the DNA template and expel the oligonucleotide from the sense DNA strand. Indeed, the intensity of those bands at low molecular weight decreased for both oligonucleotides (see Appendix X, Figure A.11) supporting the previously described mechanism. What is more, the intensity of these bands when using the antisense T7 oligonucleotide decreased to a further extent than with the 3T17_T7 oligonucleotide which is also comprehensive due to the increased instability of the hybridization between the sense DNA strand and this oligonucleotide due to the TFO portion of the sequence.

Although effective in inhibiting the expression of a gene *in vitro*, this mechanism of silencing is not ideal. Transcription occurs inside the nucleus of cells and thus the inhibitory oligonucleotides – to be delivered in the cytoplasm – would have to translocate to the nucleus to perform the inhibition, enhancing the difficulty of the system and lessening the chances of significant gene repression.

The inhibition of gene expression at the post-transcriptional level bypasses this barrier, turning itself as more feasible and less intricate.

3.3.2. Inhibition of *in vitro* translation via antisense DNA

To suppress *in vitro* translation, an antisense oligonucleotide complementary to the Shine-Dalgarno sequence (i.e. the ribosome binding site – RBS) and to the start codon was used, – 3T17_RBS (see Table 2.1 for sequence) – accomplishing inhibition by hindrance of both ribosome access and initiation of translation. This oligonucleotide has also the same TFO sequence as 3T17_T7 used for inhibition of *in vitro* transcription that will not contribute to the inhibition. 3T17_RBS is actually an extension of the 3T17 oligonucleotide: 3T17 has only 10 nucleotides complementary to the RBS in order to increase T17 structure stability whereas 3T17_RBS has additional 10 nucleotides. This oligonucleotide contains the complete RBS antisense sequence (20 nucleotides) plus the TFO sequence (17 nucleotides). The system used to assess inhibition by 3T17_RBS oligonucleotide was a plasmid with the gene encoding GFP and *E. coli* lysate for conjugation of the plasmid in order to have every component of a cell's machinery. The percentage of translation was determined as a function of fluorescence emission by GFP after incubation with discrete concentrations of 3T17_RBS (Figure 3.12).

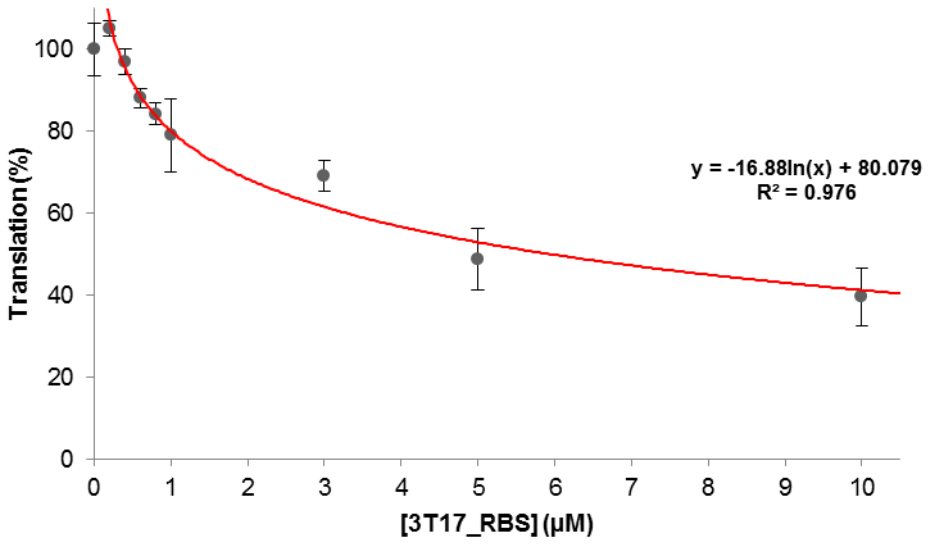

Figure 3.12 – Inhibition of *in vitro* translation. *In vitro* translation levels measured as fluorescence of GFP after incubation with discrete concentrations of 3T17_RBS. Error bars correspond to average and standard deviation of three assays. Red line corresponds to the trend line of the results discarding the 0 μM point.

Fluorescence measured from GFP decreased by about 60% after incubation with 10 μM of 3T17_RBS. There is a clear correlation between the concentration of inhibitory oligonucleotide used in the assay, and the decrease of emission from GFP and therefore, diminution of translation. However, even at high concentrations of 3T17_RBS (10 μM), *in vitro* translation was not fully blocked as in the *in vitro* transcription assay with lower oligonucleotide concentration (5 μM). This might be due to the DNases and RNases present in the *E. coli* lysate that are possibly causing degradation of a percentage of the naked oligonucleotide in the assay. Nonspecific nucleases quickly digest unmodified oligonucleotides in most biological fluids, rendering them less effective (Galderisi *et al.*, 1999). Degradation did not occur in *in vitro* transcription assays because it was done with purified PCR

product, dampening significantly the amount of nucleases present in the medium. If *in vitro* transcription was followed by the same system, it would have perhaps been less effective in silencing expression than it was in a more innocuous system. It is important to note, however, that the final system of silencing includes functionalization of a DNA construct to AuNPs. The protection against nuclease digestion of nucleic acids functionalized onto AuNPs' surface has already been verified (Rosi *et al.*, 2006; Conde *et al.*, 2010; Prigodich *et al.*, 2011) supporting the use of AuNPs as vectors to attain a high yield silencing of gene expression. Achieving gene silencing by the use of antisense oligonucleotides directly conjugated with AuNPs has been previously reported (Rosi *et al.*, 2006; Conde *et al.*, 2010) with positive results.

4. Conclusion

The present work describes the development of a gene silencing system in which a triplex DNA structure containing a therapeutic oligonucleotide stabilized by Hoogsteen hydrogen bonds is functionalized onto the AuNPs' surface. The therapeutic oligonucleotide is to be released from the AuNPs upon increase in the temperature by laser irradiation. In its free form, the therapeutic oligonucleotide will be able to silence the expression of a gene of interest. The three main parts of this project (structure formation, AuNP vectorization, and gene silencing) were assessed in parallel and several conclusions can be drawn considering the obtained results.

The first task was to build a complex structure of DNA (named T17 structure) that was composed by a double stranded portion and a therapeutic oligonucleotide to be released by thermal denaturation. This third oligonucleotide was bond to one of the strands of the dsDNA by Hoogsteen base pairing that would allow the release at lower temperatures that the conventional Watson-Crick base pairing. The formation of T17 structure was attempted in physiological pH (7.6 in 10 mM Tris-HCl) and different concentrations of $MgCl_2$ and/or NaCl. Other divalent cations were also screened although an extensive analysis was not performed. The assessment of T17 structure formation was performed mainly by fluorescence spectroscopy (FRET analysis) and UV melting profiles. In order to follow the construction by FRET, labeling of two out of the three oligonucleotides was performed with two fluorescein derivatives (FAM and JOE). Emission spectra revealed direct excitation of the acceptor fluorophore rendering the analysis inconclusive. To circumvent this issue, an analysis using excitation spectra instead was employed. The measured spectra revealed that when two conditions seemed to reveal the T17 structure assemble: 10 mM $MgCl_2$ and 10 mM $MgCl_2$ 50 mM NaCl. Changing of the fluorophores to suppress the direct excitation would lead to a more straightforward analysis.

Following absorption at 260 nm changes with the gradual increase of temperature also revealed that T17 might have formed when 10 mM $MgCl_2$ is present in the medium since two transitions were observed.

AuNPs were the vector of choice to functionalize the T17 construct. At first, double stranded functionalization to AuNPs was attempted via conjugation with the thiol group of one of the strands. Several methods of functionalization of dsDNA onto the AuNPs' surface were tested in order to find the best conditions of conjugation since an optimized method for dsDNA functionalization to AuNPs is not yet well established. The best results were attained by adapting the protocol described by Hurst and colleagues (Hurst *et al.*, 2006) but functionalization in dsDNA was still poor. To overcome this, three strategies could be employed:

1) Thiolate both strands in order to avoid removal of the indirectly functionalized oligonucleotide upon salt addition and temperature denaturation caused by sonication;
2) Avoid sonication during synthesis of dsDNA-AuNP conjugates;
3) Or functionalize only the thiolated strand and instead of having a three-stranded construct, create a double helix paired only by Hoogsteen hydrogen bonds.

The last hypothesis would also decrease the steric hindrance at the AuNPs surface.

The final main task was the silencing *in vitro* transcription and *in vitro* translation by an antisense oligonucleotide strategy. In the present work is demonstrated that oligonucleotides not fully complementary to the target sequence (T7 promoter for *in vitro* transcription and RBS and start codon for *in vitro* translation) were able to silence these cellular processes.

The full system remains to be tested and fully developed. Nonetheless, these results prove the feasibility of these oligonucleotides to significant block transcription and translation machinery in its naked form in a nuclease-rich medium (in the case of inhibition of *in vitro* translation) so they will have an even higher yield of blockage when protected by AuNPs.

Many milestones have been accomplished given the little time available but, undoubtedly, there are still many obstacles to be overcome in order to achieve the planned system of delivery. However, much light has been shed regarding the formation of triplex DNA and its stability under physiological conditions. Perhaps base analogs or stabilizing molecules compatible with physiologic conditions should be used as an aid to form more stable structures without compromising the release of the TFO by a mild raise of temperature.

Many questions are yet to be answered, e.g.:

- Is the structure really being formed?
- Is it better to have two oligonucleotides stabilized by Hoogsteen hydrogen bonds (1T17 and 3T17 oligonucleotides) rather than the T17 structure?
- What is the best way to achieve a high yield loading of dsDNA onto AuNPs?
- Is it possible to follow the same functionalization protocol to load tsDNA or this structure is too unstable to cope with the high NaCl concentrations?

These questions will hopefully be answered in future projects until the system is fully operational. It is important to stress that the envisioned system can in principle be applied to a plethora of other targets for minimally invasive nanomedical purposes.

5. References

Bagalkot, V., Zhang, L., Levy-Nissenbaum, E., Jon, S., Kantoff, P.W., Langer, R. and Farokhzad, O.C. 2007. Quantum dot-aptamer conjugates for synchronous cancer imaging, therapy, and sensing of drug delivery based on bi-fluorescence resonance energy transfer. Nano Lett. 7(10):3065-3070.

Baptista, P., Pereira, E., Eaton, P., Doria, G., Miranda, A., Gomes, I., Quaresma, P. and Franco, R. 2008. Gold nanoparticles for the development of clinical diagnosis methods. Anal. Bioanal. Chem. 391:943-950.

Bardhan, R., Lal, S., Joshi, A. and Halas, N.J. 2011. Theranostic nanoshells: from probe design to imaging and treatment of cancer. Acc. Chem. Res. 44(10):936-946.

Boisselier, E. and Astruc, D. 2009. Gold nanoparticles in nanomedicine: preparations, imaging, diagnostics, therapies and toxicity. Chem. Soc. Rev. 38:1759-1782.

Chan, P.P. and Glazer, P.M. 1997. Triplex DNA: fundamentals, advances, and potential applications for gene therapy. J. Mol. Med. 75:267-282.

Chen, P.C., Mwakwari, S.C. and Oyelere, A. 2008. Gold nanoparticles: from nanomedicine to nanosensing. Nanotechnology, Science and Applications 1:45-66.

Cheng, S.-H., Lee, C.-H., Yang, C.-S., Tseng, F.-G., Mou, C.-Y. and Lo, L.-W. 2009. Mesoporous silica nanoparticles functionalized with an oxygen-sensing probe for cell photodynamic therapy: potential cancer theranostics. J. Mater. Chem. 19:1252-1257.

Chiou, C.-C., Chen, S.-W., Luo, J.-D. and Chien, Y.-T. 2011. Monitoring triplex DNA formation with fluorescence resonance energy transfer between a fluorophore-labeled probe and intercalating dyes. Anal. Biochem. 416(1):1-7.

Chiou, C.-C., Chen, S.-W., Luo, J.-D. and Chien, Y.T. Monitoring triplex DNA formation with fluorescence resonance energy transfer between a fluorophore-labeled probe and intercalating dyes. Anal. Biochem. 416(1):1-7.

Conde, J., de la Fuente, J.M. and Baptista, P.V. 2010. In vitro transcription and translation inhibition via DNA functionalized gold nanoparticles. Nanotechnology. 21:505101-505106.

Dallas, A. and Vlassov, A.V. 2006. RNAi: A novel antisense technology and its therapeutic potential. Med. Sci. Monit. 12(4):RA67-74.

De Paula, D., Bentley, M.V. and Mahato, R.I. 2007. Hydrophobization and bioconjugation for enhanced siRNA delivery and targeting. RNA 13:431-456.

de Fougerolles, A., Vornlocher, H.P., Maraganore, J. and Lieberman, J. 2007. Interfering with disease: a progress report on siRNA-based therapeutics. Nat. Rev. Drug Discov. 6:443–453.

Debin, A., Laboulais, C., Ouali, M., Malvy, C., Le Bret, M. and Svinarchuk. 1999. Stability of G,A triple helices. Nucleic Acids Res. 27(13):2699-2707.

Demers, L.M., Mirkin, C.A., Mucic, R.C., Reynolds, R.A., Letsinger, R.L., Elghanian, R. and Viswanadham, G. 2000. A fluorescence-based method for determining the surface coverage and hybridization efficiency of thiol-capped oligonucleotides bound to gold thin films and nanoparticles. Anal. Chem. 72(22):5535-5541.

Duca, M., Vekhoff, P., Oussedik, K., Halby, L., and Arimondo, P.B. 2008. The triple helix: 50 years later, the outcome. Nucleic Acids Res. 36(16):5123-5138.

Durniak, K.J., Bailey, S. and Steitz, T.A. 2008. The structure of a transcribing T7 RNA polymerase in transition from initiation to elongation. Science. 322:553-557.

El-Sayed, M.A. 2001. Some interesting properties of metals confined in time and nanometer space of different shapes. Accounts Chem. Res. 34(4):257-264.

Elsner, H.I. and Lindblad, E.B. 1989. Ultrasonic degradation of DNA. DNA. 8(10):697-701.

Eustis, S. and El-Sayed, M.A. 2006. Why gold nanoparticles are more precious than pretty gold: Noble metal surface plasmon resonance and its enhancement of the radiative and nonradiative properties of nanocrystals of different shapes. Chem. Soc. Rev. 35:209-217.

Ferrari, M. 2005. Cancer nanotechnology: opportunities and challenges. Nat. Rev. Cancer 5:161-171.

Fox, K.R. and Brown, T. 2011. Formation of stable DNA triplexes. Biochem. Soc. Trans. 39:629–634.

Frank-Kamenetskii, M.D. and Mirkin, S.M. 1995. Triplex DNA structures. Annu. Rev. Biochem. 64:65-95.

Galderisi, U., Cascino, A. and Giordano, A. 1999. Antisense oligonucleotides as therapeutic agents. J. Cell. Physiol. 181:251-257.

Ghosh, P., Han, G., De, M., Kim, C.K. and Rotello,V.M. 2008. Gold nanoparticles in delivery applications. Adv. Drug Deliver. Rev. 60: 1307–1315.

Gianella, A., Jarzyna, P.A., Mani, V., Ramachandran, S., Calcagno, C., Tang, J., Kann, B., Dijk, W.J.R., Thijssen, V.L., Griffioen, A.W., Storm, G., Fayad, Z.A. and Mulder, W.J.M. 2011. Multifunctional nanoemulsion platform for imaging guided therapy evaluated in experimental cancer. ACS Nano 5(6):4422-4433.

Giljohann, D.A., Seferos, D.S., Prigodich, A.E., Patel, P.C. and Mirkin, C.A. 2009. Gene regulation with polyvalent siRNA-nanoparticle conjugates. J. Am. Chem. Soc. 131:2072-2073.

Govorov, A.O. and Richardson, H.H. 2007. Generating heat with metal nanoparticles. Nano Today 2(1):30-38.

Govorov, A.O., Zhang, W., Skeini, T., Richardson, H., Lee, J. and Kotov, N.A. 2006. Gold nanoparticle ensembles as heaters and actuators: melting and collective plasmon resonances. Nanoscale Res. Lett. 1:84-90.

Hammond, S.M., Caudy, A.A. and Hannon, G.J. 2001. Post-transcriptional gene silencing by double-stranded RNA. Nat. Rev. Genet. 2:110-119.

Han, G., You, C.-C., Kim, B.-J., Turingan, R.S., Forbes, N.S., Martin, C.T. and Rotello, V.M. 2006. Light-regulated release of DNA and its delivery to nuclei by means of photolabile gold nanoparticles. Angew. Chem. 118: 3237 –3241.

Han, X., Li, Y., Wu, S. and Deng, Z. 2008. A general strategy toward pH-controlled aggregation-dispersion of gold nanoparticles and single-walled carbon nanotubes. Small. 4(3):326-329.

Hannon, G.J. and Rossi, J.J. 2004. Unlocking the potential of the human genome with RNA interference. Nature 431:371-378.

Ho, Y. and Leong, K.W. 2010. Quantum dot-based theranostics. Nanoscale 2:60-68.

Hu, M., Chen, J., Li, Z.H., Au, L., Hartland, G.V., Li, X., Marquez, M. and Xia, Y. 2006. Gold nanostructures: engineering their plasmonic properties for biomedical applications. Chem. Soc. Rev. 35:1084-1094.

Huang, X., El-Sayed, M.A. 2010. Gold nanoparticles: Optical properties and implementations in cancer diagnosis and photothermal therapy. Journal of Advanced Research 1:13-28.

Hurst, S.J., Lytton-Jean, A.K.R. and Mirkin, C.A. 2006. Maximizing DNA loading on a range of gold nanoparticle sizes. Anal. Chem. 78(24):8313-8318.

Huschka, R., Neumann, O., Barhoumi, A. and Halas, N.J. 2010. Visualizing light-triggered release of molecules inside living cells. Nano Lett. 10(10):4117-4122.

Jain, A., Wang, G. and Vasquez, K.M. 2008. DNA triple helices: Biological consequences and therapeutic potential. Biochimie 90:1117-1130.

Jain, P.K., Huang, X., El-Sayed, I.H. and El-Sayed, M.A. 2007. Review of Some Interesting Surface Plasmon Resonance-enhanced Properties of Noble Metal Nanoparticles and Their Applications to Biosystems. Plasmonics 2:107-118.

Jain, P.K., Huang, X., El-Sayed, I.H. and El-Sayed, M.A. 2008. Noble metals on the nanoscale: optical and photothermal properties and some applications in imaging, sensing, biology, and medicine. Acc. Chem. Res. 41(12):1578-1586.

Jain, P.K., Lee, K.S., El-Sayed, I.H. and El-Sayed, M.A. 2006. Calculated absorption and scattering properties of gold nanoparticles of different size, shape, and composition: applications in biological imaging and biomedicine. J. Phys. Chem. B 110: 7238-7248.

Kato, G.J. and Dang, C.V. 1992. Function of the c-Myc oncoprotein. FASEB J. 6:3065-3072.

Ke, H., Wang, J., Dai, Z., Jin, Y., Qu, E., Xing, Z., Guo, C., Yue, X. and Liu, J. 2011. Gold-nanoshelled microcapsules: a theranostic agent for ultrasound contrast imaging and photothermal therapy. Angew. Chem. Int. Ed. 50:3017–3021.

Kim, S.H., Jeonga, J.H., Choa, K.C., Kimb, S.W. and Park, T.G. 2005. Target-specific gene silencing by siRNA plasmid DNA complexed with folate-modified poly(ethylenimine). J. Control. Release 104:223-232.

Knuaert, M.P. and Glazer, P.M. 2001. Triplex forming oligonucleotides: sequence-specific tools for gene targeting. Hum. Mol. Genet. 10(20):2243-2251.

Kotov, N.A. and Stellacci, F. 2008. Frontiers in nanoparticle research: toward greater complexity of structure and function of nanomaterials. Adv. Mater. 20:4221–4222.

Larguinho, M., Santos, H.M., Doria, G., Scholzb, H., Baptista, P.V. and Capelo, J.L. 2010. Development of a fast and efficient ultrasonic-based strategy for DNA fragmentation. Talanta. 81:881-886.

Lee, J.E., Kim, T., Kim, S.Y. and Kim, S.W. 2010. Detection of triple helix DNA formation of guanine-rich oligonucleotide in sodium ion abundant buffer by cross-checking FRET scheme. Chem. Phys. Lett. 490:230-233.

Lee, P.C. and Meisel, D. 1982. Adsorption and surface-enhanced Raman of dyes on silver and gold sols. J. Phys. Chem. 86:3391-3395.

Lewin, B. 2007. Genes IX. 9th ed. Jones & Bartlett Publishers Inc.: Sudbury, Massachusetts. p 343-344.

Liu, Y., Shipton, M.K., Ryan, J., Kaufman, E.D., Franzen, S. and Feldheim, D.L. 2007. Synthesis, stability, and cellular internalization of gold nanoparticles containing mixed peptide-poly(ethylene glycol) monolayers. Anal. Chem. 79(6):2221-2229.

Lukianova-Hleb, E.Y., Hanna, E.Y., Hafner, J.H. and Lapotko, D.O. 2010. Tunable plasmonic nanobubbles for cell theranostics. Nanotechnology 21:085102.

Malkov, V.A., Voloshin, O.N., Soyfer, V.N. and Frank-Kamenetskii, M.D. 1993. Cation and sequence effects on stability of intermolecular pyrimidine-purine-purine triplex. Nucleic Acids Res. 21(3):585-591.

McIntosh, C.M., Esposito, E.A., Boal, A.K., Simard, J.M., Martin, C.T. and Rotello, V.M. 2001. Inhibition of DNA transcription using cationic mixed monolayer protected gold clusters. J. Am. Chem. Soc. 123:7626-7629.

Medarova, Z., Pham, W., Farrar, C., Petkova, V. and Moore, A. 2007. *In vivo* imaging of siRNA delivery and silencing in tumors. Nat. Med. 13(3):372-377.

Meister, G. and Tuschl, T. 2004. Mechanisms of gene silencing by double-stranded RNA. Nature 431:343-349.

Melancon, M.P., Zhou, M. and Li, C. 2011. Cancer theranostics with near-infrared light-activatable multimodal nanoparticles. Acc. Chem. Res. 44(10):947-956.

Mukherjee, A. and Vasquez, K.M. 2011. Triplex technology in studies of DNA damage, DNA repair, and mutagenesis. Biochimie. 93(8):1197-1208.

Murphy, C.J., Gole, A.M., Stone, J.W., Sisco, P.N., Alkilany, A.M., Goldsmith, E.C. and Baxter, S.C. 2008. Gold Nanoparticles in Biology: Beyond Toxicity to Cellular Imaging. Acc. Chem. Res. 41(12):1721-1730.

Niemeyer, C.M. and Mirkin, C.A. 2004. Nanobiotechnology: Concepts, applications and perspectives. 1st ed., Wiley-VCH, Weinheim.

Oliveira, S., Storm, G. and Schiffelers, R.M. 2006. Targeted delivery of siRNA. J. Biomed. Biotechnol. 2006:1-9.

Park, J.H., von Maltzahn, G., Ruoslahti, E., Bhatia, S.N. and Sailor, M.J. 2008. Micellar hybrid nanoparticles for simultaneous magnetofluorescent imaging and drug delivery. Angew. Chem. Int. Ed. 47:7284-7288.

Patil, S.D., Rhodes, D.G. and Burgess, D.J. 2005. DNA-based therapeutics and dna delivery systems: a comprehensive review. AAPS J. 7:E61-E77.

Pellegrino,T., Sperling, R.A., Alivisatos, A.P. and Parak, W.J. 2007. Gel Electrophoresis of Gold-DNA Nanoconjugates. J. Biomed. Biotechnol. 2007:26796-26805.

Pirollo, K.F. and Chang, E. 2008. Targeted Delivery of Small Interfering RNA: Approaching Effective Cancer Therapies. Cancer Res. 68(5):1247-1250.

Plum, G.E., Park, Y.-W., Singleton, S.F. and Dervan, P.B. 1990. Thermodynamic characterization of the stability and the melting behavior of a DNA triplex: A spectroscopic and calorimetric study. Proc. Nati. Acad. Sci. USA. 87:9436-9440.

Poon, L., Zandberg, W., Hsiao, D., Erno, Z., Sen, D., Gates, B.D. and Branda, N.R. 2010. Photothermal release of single-stranded DNA from the surface of gold nanoparticles through controlled denaturating and Au−S bond breaking. ACS Nano 4(11):6395-6403.

Prigodich, A.E., Alhasan, A.H. and Mirkin, C.A. 2011. Selective enhancement of nucleases by polyvalent DNA-functionalized gold nanoparticles. J. Am. Chem. Soc. 133:2120-2123.

Prigodich, A.E., Seferos, D.S., Massich, M.D., Giljohann, D.A., Lane, B.C. and Mirkin, C.A. 2009. Nano-flares for mRNA Regulation and Detection. ACS Nano 3(8):2147-2152.

Rayburn, E.R. and Zhang, R. 2008. Antisense, RNAi, and gene silencing strategies for therapy: Mission possible or impossible? Drug Discov. Today. 13:513-521.

Reither, S. and Jeltsch, A. 2002. Specificity of DNA triple helix formation analyzed by a FRET assay. BMC Biochem. 3:27-35.

Rong, M., He, B., Mcallister, W.T. and Durbin, R.K. 1998. Promoter specificity determinants of T7 RNA polymerase. Proc. Natl. Acad. Sci. USA. 95:515-519.

Rosi, N.L., Giljohann, D.A., Thaxton, C.S., Lytton-Jean, A.K.R., Han, M.S. and Mirkin, C.A. 2006. Oligonucleotide-modified gold nanoparticles for intracellular gene regulation. Science 312:1027-1030.

Rusling, D.A., Rachwal, P.A., Brown, T. and Fox, K.R. 2009. The stability of triplex DNA is affected by the stability of the underlying duplex. Biophys. Chem. 145:105-110.

Salata, O.V. 2004. Applications of nanoparticles in biology and medicine. J. Nanobiotechnol. 2(3).

Sato, K., Hosokawa, K. and Maeda, M. 2003. Rapid aggregation of gold nanoparticles induced by non-cross-linking DNA hybridization. J. Am. Chem. Soc. 125(27):8102-8103.

Scaria, P.V. and Shafer, R.H. 1996. Calorimetric analysis of triple helices targeted to the d(G3A4G3)•(C3T4C3) duplex. Biochemistry. 35:10985-10994.

Schneider, U.V., Severinsen, J.K., Géci, I., Okkels, L.M., Jøhnk, N., Mikkelsen, N.D., Klinge, T., Pedersen, E.B., Westh, H. and Lisby, G. 2010. A novel FRET pair for detection of parallel DNA triplexes by the LightCycler. BMC Biotechnology. 10:4-15.

Somia, N. and Verma, I.M. 2000. Gene therapy: trials and tribulations. Nat. Rev. Genet. 1:91-99.

Sperling, R.A., Gil, P.R., Zhang, F., Zanella, M. and Parak, W.J. 2008. Biological applications of gold nanoparticles. Chem. Soc. Rev. 37:1896-1908.

Su, K.-H., Wei, Q.-H., Zhang, X., Mock, J.J., Smith, D.R. and Schultz, S. 2003. Interparticle coupling effects on plasmon resonances of nanogold particles. Nano Lett. 3:1087-1090.

Sugimoto, N., Wu, P., Hara, H. and Kawamoto, Y. 2001. pH and cation effects on the properties of parallel pyrimidine motif DNA triplexes. Biochemistry. 40:9396-9405.

Tamm, I., Dorken, B. and Hartmann, G. 2001. Antisense therapy in oncology: new hope for an old idea? Lancet 358(9280):489-497.

Waehler, R., Russell, S.J. and Curiel, D.T. 2007. Engineering targeted viral vectors for gene therapy. Nat. Rev. Genet. 8:573-587.

Wan, C., Cui, M., Song, F., Liu, Z. and Liu, S. 2009. Evaluation of effects of bivalent cations on the formation of purine-rich triple-helix DNA by ESI-FT-MS. J. Am. Mass Spectrom. 20:1281-1286.

Wasylishen, A.R. and Penn, L.Z. 2010. Myc : The Beauty and the Beast. Genes & Cancer. 1(6):532-541.

Whitehead, K.A., Langer, R. and Anderson, D.G. 2009. Knocking down barriers: advances in siRNA delivery. Nat. Rev. Drug Discov. 8:129-138.

Wilson, R. 2008. The use of gold nanoparticles in diagnostics and detection. Chem. Soc. Rev. 37:2028-2045.

Wu, P., Kawamotob, Y., Harab, H. and Sugimoto, N. 2002. E ffect of divalent cations and cytosine protonation on thermodynamic properties of intermolecular DNA double and triple helices. J. Inorg. Biochem. 91:277-285.

Xie, J., Lee, S. and Chen, X. 2010. Nanoparticle-based theranostic agents. Adv. Drug Deliver. Rev. 62:1064-1079.

Yezhelyev, M.V., Qi, L., O'Regan, R.M., Nie, S. and Gao, X. 2008. Proton-sponge coated quantum dots for siRNA delivery and intracellular imaging. J. Am. Chem. Soc. 130:9006-9012.

Yin, Y.W. and Steitz, T.A. 2002. Structural basis for the transition from initiation to elongation transcription in T7 RNA polymerase. Science. 298:1387-1395.

Yin, Y.W. and Steitz, T.A. 2004. The structural mechanism of translocation and helicase activity in T7 RNA polymerase. Cell. 116:393-404.

6. Appendices

Appendix I – PAGE analysis

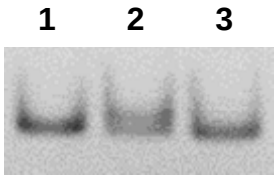

Figure A.1 – 12% non-denaturing PAGE in 17.8 mM Tris-borate (pH 7.2) and 10 mM $MgCl_2$. Lanes: 1 – 1T17 + 2T17; 2 – T17 structure (1T17 + 2T17 + 3T17); 3 – 1T17 + 2T17 + non-TFO. For the sequences of these oligonucleotides refer to Table 2.1 in the Material and Methods section. PAGE was run at 70 V at 4ºC for 2 hours and 30 minutes. The gel was then stained with ethidium bromide. The gel should had be run for a longer time in order to understand if lane 2 shows two gel bands (and therefore evidences the presence of the T17 structure as well as the presence of the double helix) or only one broader gel band, corresponding to the double helix formed by 1T17 and 2T17 oligonucleotides.

Appendix II – FRET efficiency calculation

The FRET efficiency (E) is the fraction of photons absorbed by the donor which are then transferred to the acceptor. This fraction can be given by the following equation:

$$E = \frac{1}{1+\left(\frac{r}{R_0}\right)^6} \qquad \text{Equation 1}$$

where R_0 is the Förster distance (distance at which energy transfer efficiency is 50% between the donor and acceptor) and r is the donor-acceptor distance. As the distance between donor and acceptor decreases, the FRET efficiency increases.
The R_0 can be calculated through the following equation:

$$R_0^6 = 8.79\times10^{23}\ \Phi_D\ \kappa^2 n^{-4} J(\lambda) \qquad \text{Equation 2}$$

Φ_D is the quantum yield of the donor, κ is the dipole orientation factor (typically $\kappa^2 = 2/3$), n is the refractive index of the medium (1.33 in water) and J (in units of $M^{-1}cm^3$) is the spectral overlap integral that expresses the degree of spectral overlap between the donor emission and the acceptor absorption. This parameter can be determined by:

$$J(\lambda) = \int_0^\infty F_D(\lambda)\varepsilon_A(\lambda)\lambda^4\, d\lambda \qquad \text{Equation 3}$$

$F_D(\lambda)$ is the corrected fluorescence intensity of the donor in the wavelength range λ to λ + Δλ with the total intensity (area under the curve) normalized to unity. $\varepsilon_A(\lambda)$ is the extinction coefficient of the acceptor at λ, which is typically in units of $M^{-1}cm^{-1}$.

The J for FAM and JOE pair is 5.26×10^{-13} $M^{-1}cm^3$ and the theoretical Φ_D is 0.95. Using Equation 3, the R_0 is 67.3 Å.

The distance between this pair (r) in T17 structure is of approximately 4 nm, assuming that the width between two hybridized oligonucleotides is 2 nm for Watson-Crick hydrogen bonds and Hoogsteen hydrogen bonds. Thus, the theoretical E for this distance is approximately 95.8%.

Appendix III – Emission spectra of labeled double strand of T17 structure with labeled non-TFO

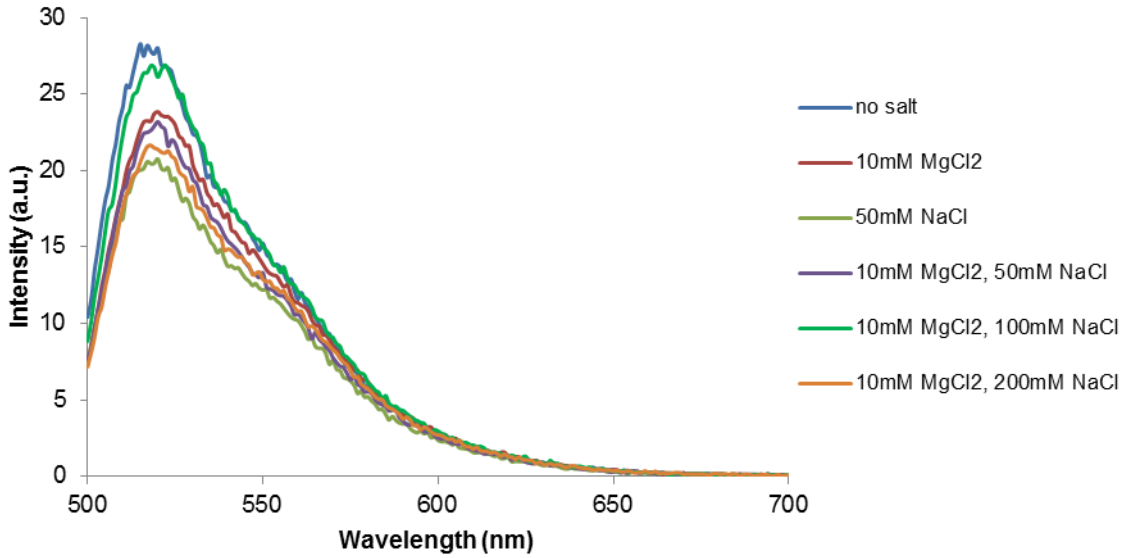

Figure A.2 – Emission spectra (λ_{exc} = 490 nm) of double helix of T17 structure (1T17 and 2T17_5'FAM) and labeled non-TFO in 10 mM Tris-HCl (pH 7.6) and different ionic conditions.

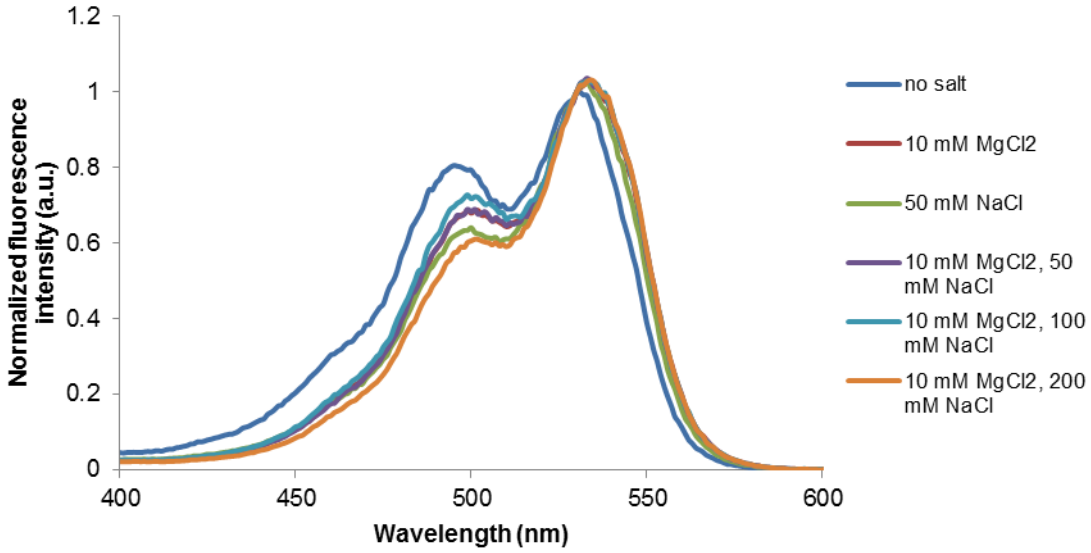

Figure A.3 – Excitation spectra (λ_{em} = 640 nm) in 10 mM Tris-HCl (pH 7.6) and different concentrations of $MgCl_2$ and/or NaCl.

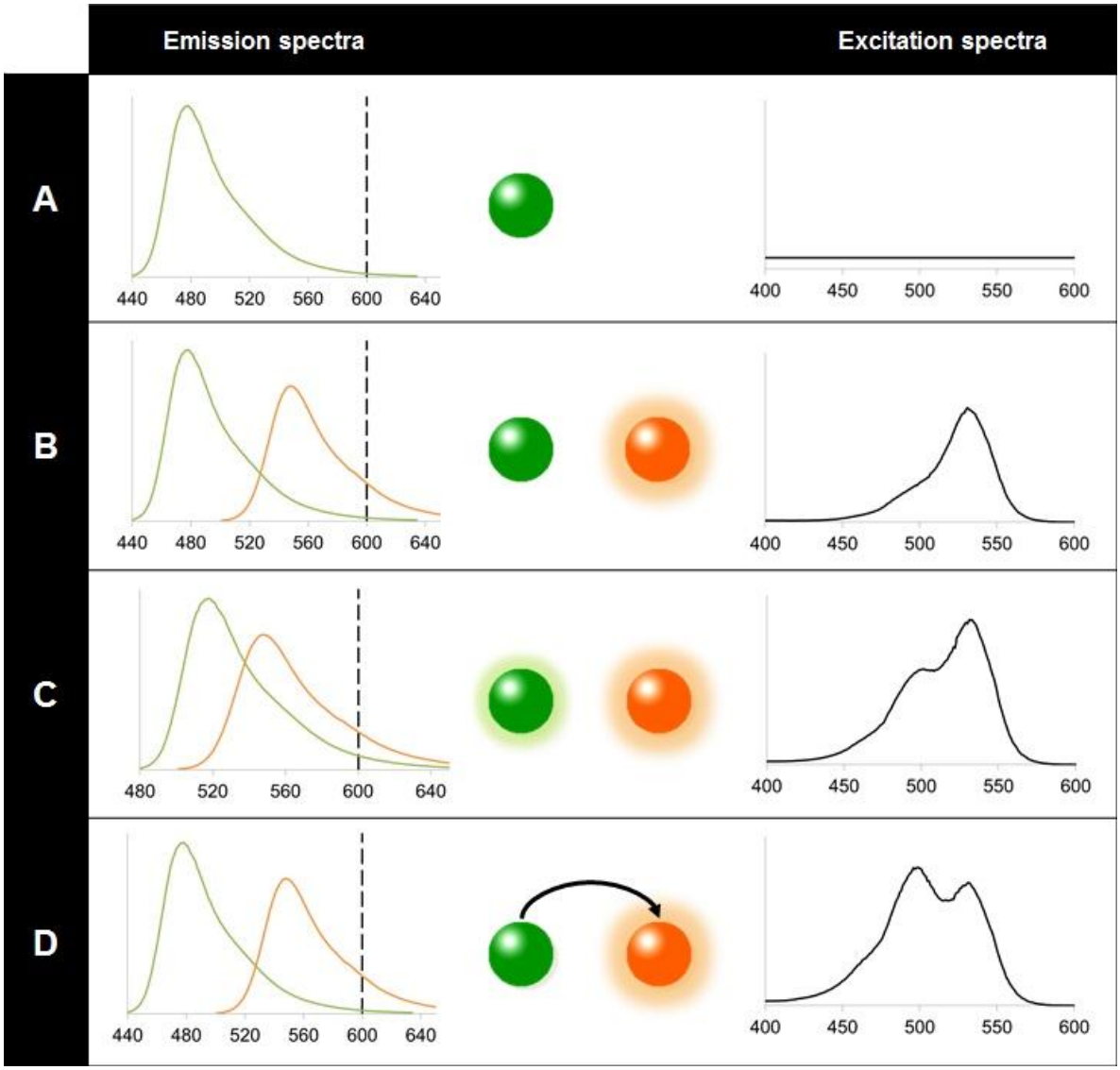

Figure A.4 – Schematic representation of emission and excitation spectra of A) one fluorophore that does not emit at the λ_{exc} set; **B)** two fluorophores that do not interact by FRET; **C)** two fluorophores that do not interact by FRET but where the green fluorophore has a residual emission at the λ_{exc} set and the orange fluorophore has a significant emission at the λ_{exc} set; **D)** two fluorophores where FRET occurs from the green fluorophore to the orange fluorophore. The dashed line indicates the λ_{exc} set. Green fluorophore: FAM; Orange fluorophore: JOE.

At the fluorescence monitoring wavelength chosen, JOE is the major responsible for emission. For simplification sake, if we consider that FAM had no emission at this wavelength, when only FAM is present in solution, no emission in the excitation spectrum would be observed (Figure A.3A), since FAM would not emit at 640 nm.

In the presence of both fluorophores but if energy transfer does not occur only the emission originated through JOE excitation would be detected (Figure A.3B). It should be noted that the emission intensity is directly proportional to the absorbance of the fluorophore, and thus the excitation spectrum of JOE should correspond to its absorption spectrum. This is the reason why the excitation spectrum maximum corresponds to JOE's maximum absorption wavelength.

Unfortunately, FAM presents non-negligible emission at 640 nm that can be observed in the excitation spectrum when both dyes are present (Figure A.3C). Here, both FAM and JOE excitation peaks can be observed at 490 nm and 530 nm, which once more, correspond to their absorption maximum. When the process of energy transfer occurs between the two fluorophores (Figure A.3D), upon FAM excitation, a percentage of that excitation will be transferred to JOE, which is able to emit photons at the monitoring wavelength. Therefore, the excitation spectra will evidence the presence of two clear peaks: one more intense at 490 nm, which corresponds to the energy transferred from FAM to JOE (plus a smaller contribution of FAM emission at 640 nm); and one at 520 nm which is originated in JOE's absorption. Excitation spectra analysis does not completely overcome the problem of direct excitation and emission cross-talk, but it offers an alternative and clearer method to split both contributions from the energy transfer one.

Appendix V – AuNPs characterization

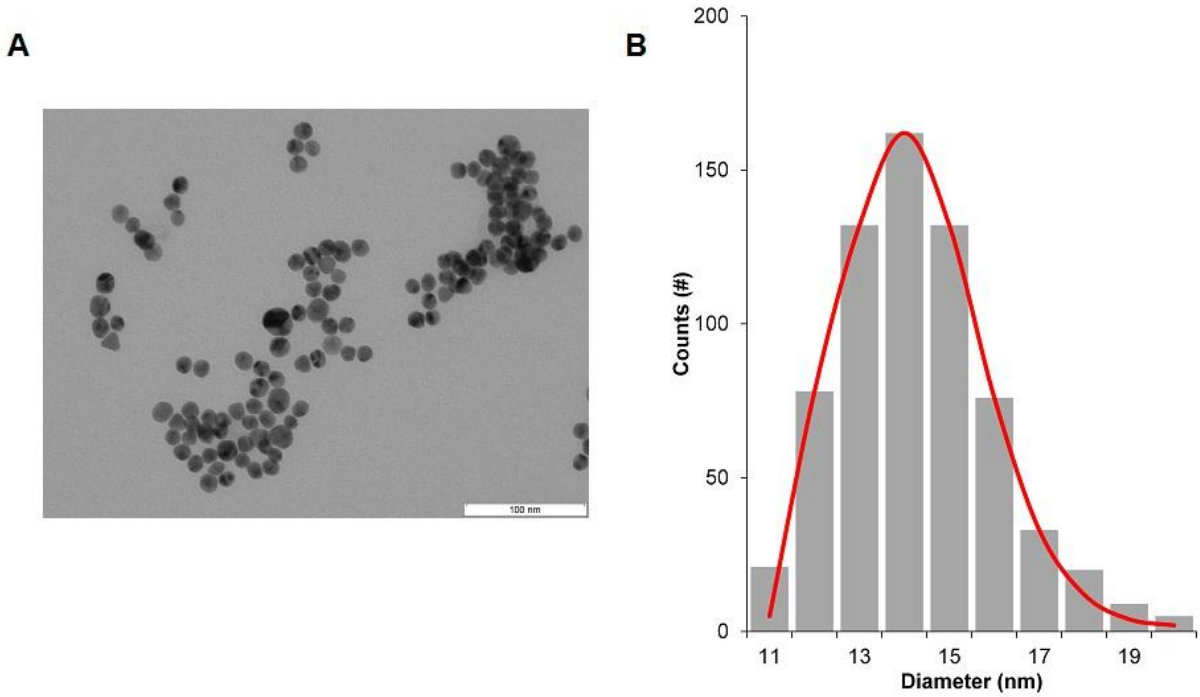

Figure A.5 – Gold nanoparticles. A) TEM image and **(B)** size histogram. AuNPs average size: 14 nm

Appendix VI – AuNPs functionalized with different concentrations of PEG

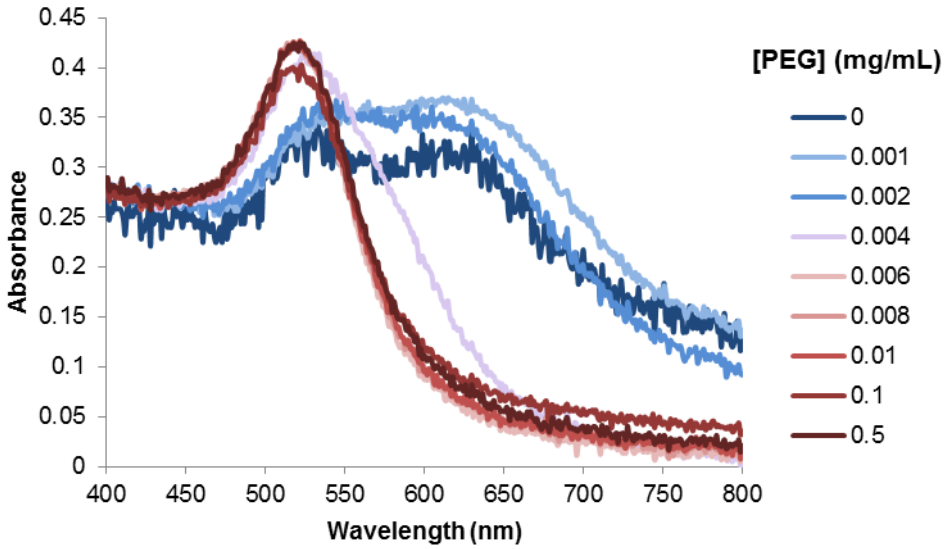

Figure A.6 – Visible spectra of AuNPs functionalized with different concentrations of PEG. Spectra represented with red lines reveal a single SPR peak at 520 nm and represent the dispersed AuNPs; and spectra represented with blue have two peaks, one at 600 nm denoting aggregation of the AuNPs and the other is slightly red-shifted from 520 nm which indicates that the aggregation is not complete.

Appendix VII – Determination of dsDNA functionalized onto the AuNPs' surface

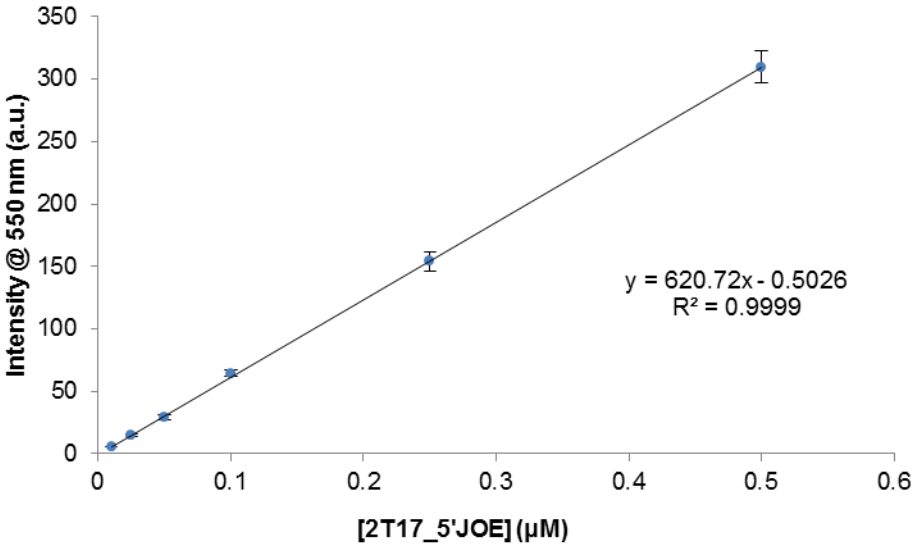

Figure A.7 – Calibration curve for quantification of 2T17_5'JOE oligonucleotide.

Table A.1 – Intensity measured at 550 nm upon excitation of the samples at 520 nm. The average and standard deviation were determined with the intensity of samples 1 and 2; sample 3 was discarded.

Sample	Intensity at 550 nm (a.u.)	Average intensity (a.u.)	Concentration (µM)
1	3.235	3.130 ± 0.150	0.006 ± 0.001
2	3.026		
3	5.201		

Appendix VIII – Determination of thiolated oligonucleotides functionalized onto AuNPs' surface

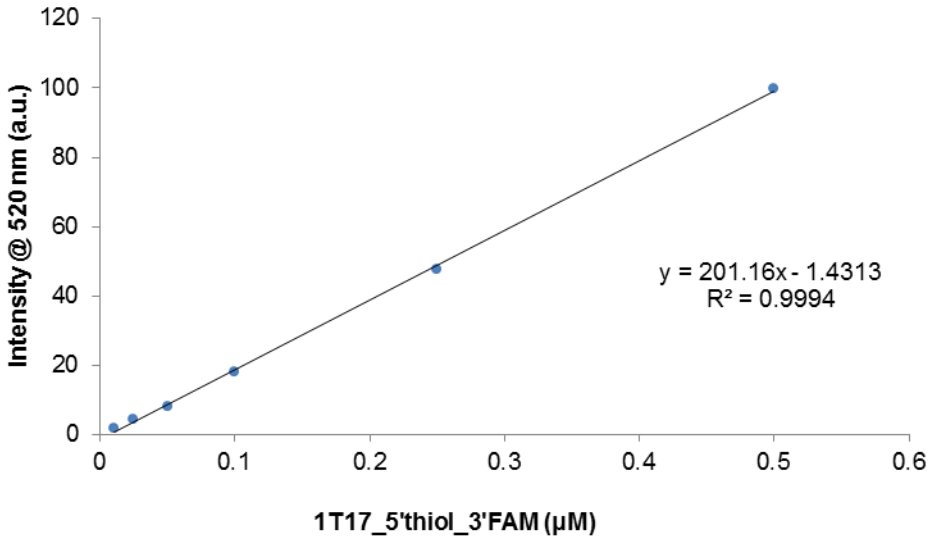

Figure A.8 – Calibration curve for quantification of 1T17_5'thiol_3'FAM oligonucleotide.

Table A.2 – Intensity measured at 520 nm upon excitation of the samples at 490 nm. The average and standard deviation were determined with the intensity of samples 1 to 3.

Sample	Intensity at 520 nm (a.u.)	Average intensity (a.u.)	Concentration (µM)
1	137.6	140.5 ± 3.5	0.706 ± 0.024
2	144.3		
3	139.5		

Appendix IX – Theoretical calculation of laser intensity to triple strand delivery from AuNPs

In the steady-state regime, the local temperature around a single spherical nanoparticle is described by the following equation:

$$\Delta T(r) = \frac{V_{NP} Q}{4\pi k_0 r} \qquad \text{Equation 4}$$

where r is the surrounding medium radius from the surface of a nanoparticle, k_0 is the thermal conductivity of the surrounding medium, and V_{NP} is the NP volume. Q is the heat generation coming from light dissipation in the nanoparticle. This value can be calculated assuming that the wavelength of the incident light is much longer that the nanoparticle radius.

$$Q = \frac{C_{abs} I_0}{V_{NP}} \qquad \text{Equation 5}$$

C_{abs} is the absorption cross-section at the laser intensity of choice for a nanoparticle with a specific radius and I_0 is the laser intensity in Wm^{-2}.

The radius of the AuNPs is $7x10^{-9}$ m, which corresponds to a volume (V_{AuNP}) of $1.44x10^{-24}$ m^3. The k_0 in the aqueous solution is 0.58 $W(m.K)^{-1}$.

The light wavelength of most lasers used for these applications is 532 nm and this is the wavelength used for this calculation. Thus, the C_{abs} for this laser wavelength and AuNP radius is approximately $1.33x10^{-16}$ m^2.

To achieve the T_m of the triplex to duplex of T17 structure (calculated as approximately 40ºC by UV melting curve), the ΔT is a 3ºC raise from physiological temperature (37ºC) at a distance of circa 8.3 nm from the surface of the AuNP. This value was calculated according to the values shown in Table A.3:

r = 0.285 + 0.182 + (6 x 0.154) + (21 x 0.33) = 8.32 nm

Table A.3 – Bond lengths used to calculate the distance from the surface of the AuNPs to the end of the triple helix in the T17 structure. The length between nucleic acid bases is 0.33 nm.

	Chemical bond length (nm)
C – C	0.154
C – S	0.182
S – Au	0.285

When a laser of $3x10^5$ W/cm^2 is used, the following theoretical increase in the temperature is verified:

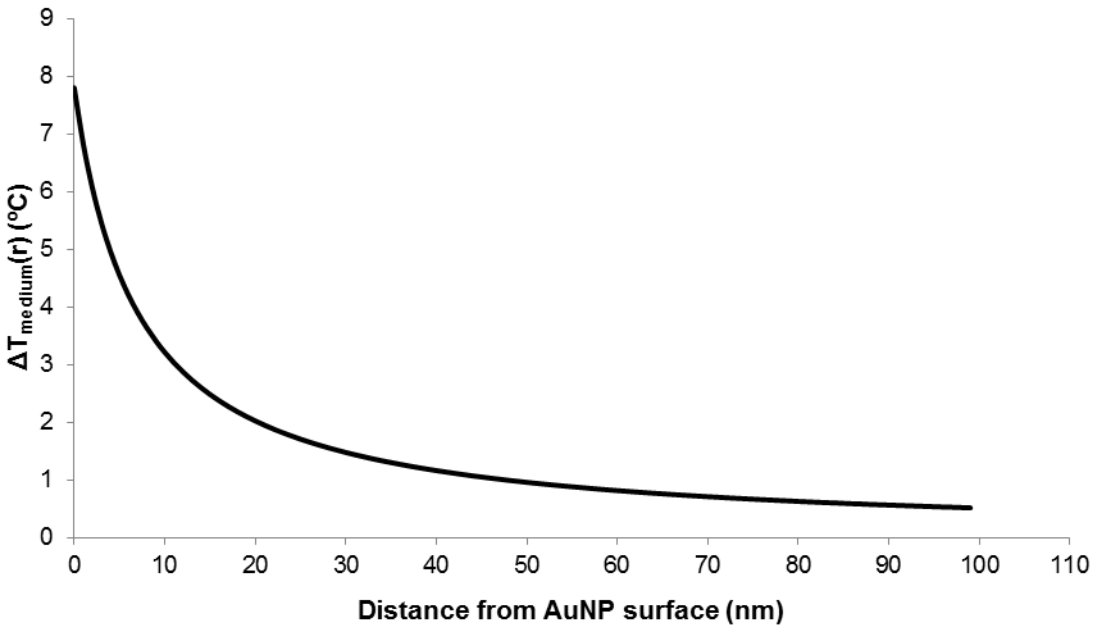

Figure A.9 – Temperature increase according to the distance from the AuNP surface when a 532 nm laser wavelength with an intensity of $3x10^5$ W/cm^2 is used. The temperature raise at a distance of 8.3 nm is approximately 4.5ºC although only a raise of 3ºC was needed, which gives a margin of error.

Appendix X – Inhibition of *in vitro* transcription: electrophoretic results

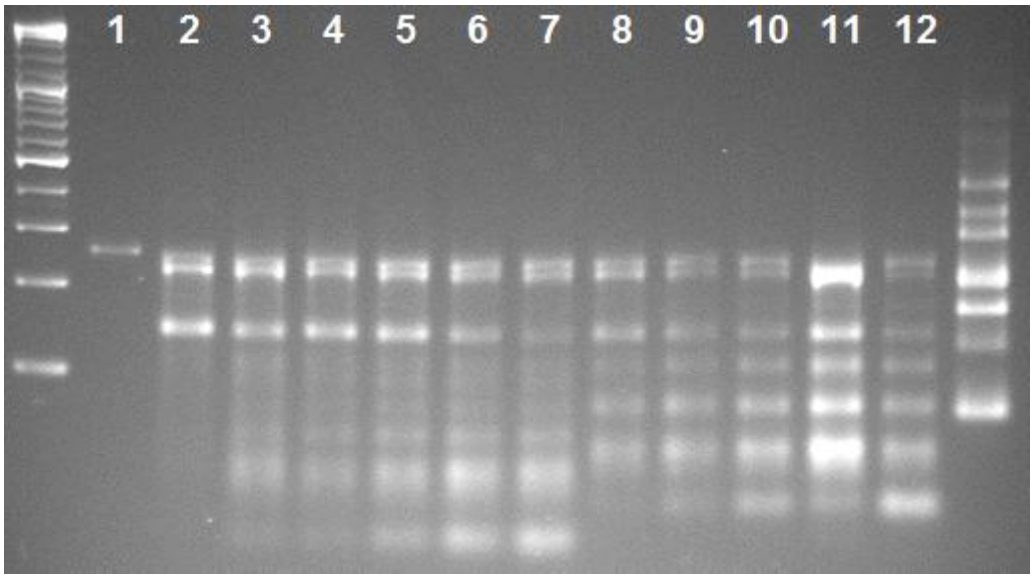

Figure A.10 – 2% agarose gel of inhibition of *in vitro* transcription without pre-hybridization of DNA template and inhibitory oligonucleotides (T7 antisense and 3T17_T7). Lanes: 1- Negative control (without T7 RNA polymerase); 2- Positive control (regular *in vitro* transcription); 3- 0.2 µM T7 antisense; 4- 0.4 µM T7 antisense; 5- 0.6 µM T7 antisense; 6- 0.8 µM T7 antisense; 7- 1 µM T7 antisense; 8- 0.2 µM 3T17_T7; 9- 0.4 µM 3T17_T7; 10- 0.6 µM 3T17_T7; 11- 0.8 µM 3T17_T7; 12- 1 µM 3T17_T7. Electrophoretic conditions: 6 V/cm, 90 min, GelRed incorporation.

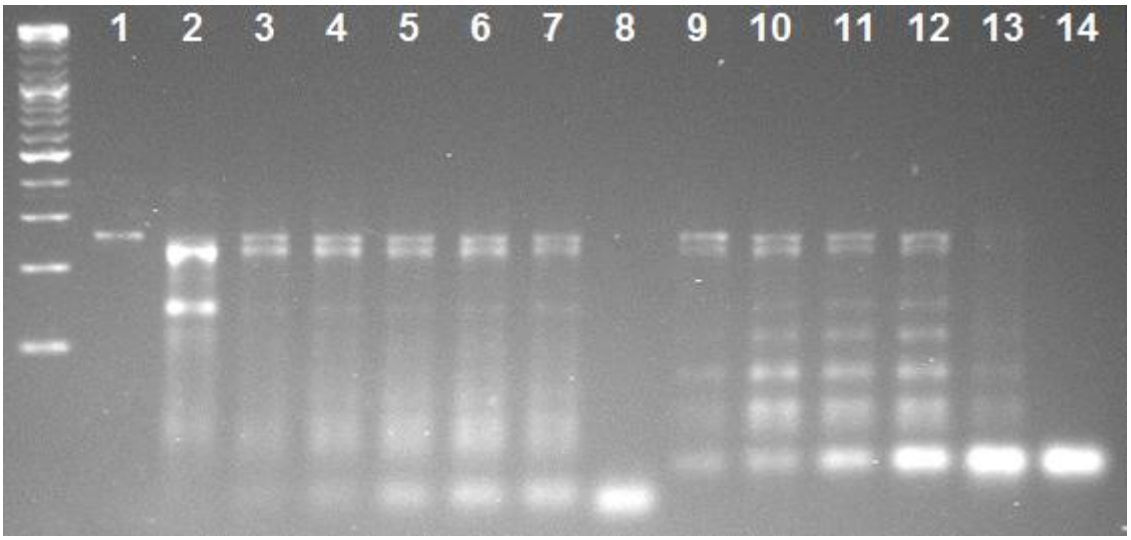

Figure A.11 – 2% agarose gel of inhibition of *in vitro* transcription with pre-hybridization of DNA template and inhibitory oligonucleotides (T7 antisense and 3T17_T7). Lanes: 1- Negative control (without T7 RNA polymerase); 2- Positive control (regular *in vitro* transcription); 3- 0.2 µM T7 antisense; 4- 0.4 µM T7 antisense; 5- 0.6 µM T7 antisense; 6- 0.8 µM T7 antisense; 7- 1 µM T7 antisense; 8- oligonucleotide control (1 µM T7 antisense) without transcription; 9- 0.2 µM 3T17_T7; 10- 0.4 µM 3T17_T7; 11- 0.6 µM 3T17_T7; 12- 0.8 µM 3T17_T7; 13- 1 µM 3T17_T7; 14- oligonucleotide control (1 µM 3T17_T7) without transcription. Electrophoretic conditions: 6 V/cm, 90 min, GelRed incorporation.